UNIVERSITY OF THESSALY

Cracked Panel Solutions in Gradient Elasticity

by

Georgios D. Tsantidis

Submitted to the Department of Mechanical Engineering

in Partial Fulfillment of the Requirements for the Degree of

MASTER OF SCIENCE

March 2010

Acknowledgments

This thesis was carried out at the Laboratory of Mechanics & Strength of Materials under the Master of Science Program of the Department of Mechanical Engineering of University of Thessaly (UTH).

I wish to express my deepest gratitude to Professor Nikolaos Aravas for his patience, guidance and encouragement. He has been more than an advisor; as a mentor he helped me grow, question and develop self confidence. I will always welcome his advice and cherish his fellowship.

I would also like to thank my officemates who provided friendship and moral support.

Last, but in no way least, I thank my wife for her love and constant support throughout the course of this work.

Contents

Chapter 1

Introduction and Literature review

The essential features of fracture mechanics began with characterizing the stress and deformation fields, in the region near the tip of a crack, in order to develop sound fracture criteria. This was achieved principally through the use of asymptotic continuum mechanics analysis where the functional form of the local singular field was determined within a scalar amplitude factor whose magnitude was calculated from a complete analysis of the applied loading and geometry. The best known example of this approach was for the linear elastic behavior of a stationary crack subjected to tensile opening (Mode I).

Classical (local) continuum theories possess no material/intrinsic length scale. The typical dimensions of length that appear are associated with the overall geometry of the domain under consideration. In spite of the fact that classical theories are quite sufficient for most applications, there is ample experimental evidence which indicates that, in certain specific applications, there is significant dependence on additional length/size parameters.

One of the most effective *generalized* (non-local) continuum theories proved to be in recent years the theory introduced by Toupin (1962) and Mindlin (1964)−see the brief literature review on applications and extensions, below. The general framework appears under the names strain-gradient theory or grade-two theory or dipolar gradient theory. This approach is appropriate for formulations of both elasticity and plasticity problems.

Historically, ideas underlying generalized continuum theories were advanced already in the 19th century by Cauchy (1851), Voigt (1887), and the brothers E. and F. Cosserat [3], but the subject was generalized and reached maturity only in the 1960's and 1970's with the works of Mindlin [14], Koiter [10][11] and Toupin [19] who considered "strain-gradient" elasticity theories, in which the elastic strain energy density is a function of strain as well as of strain and rotation gradients. They solved also a number of problems and demonstrated the effects of the material length scales that enter these theories (Mindlin and Tiersten [17], Mindlin [14][15], Koiter [11]). Several theoretical issues related to strain-gradient elasticity were addressed later by Germain [7][8][9].

The solution of a number of boundary value problems is now available in the literature (e.g. Exadaktylos [4]) including problems of fracture mechanics (e.g. Zhang *et al.* [20],

Georgiadis [6]).

The finite element implementation of "strain-gradient" constitutive models has been the subject of several publications, especially in the recent years (e.g. Amanatidou and Aravas [1]).

Regarding appropriate length scales for strain gradient theories, as noted by Zhang *et al.* [20], although strain gradient effects are associated with geometrically necessary dislocations in plasticity, they may also be important for the elastic range in microstructured materials. In elasticity, length scales enter the constitutive equations through the elastic strain energy density function W, which in this case depends not only on the strain tensor ϵ but also on gradients of the rotation ω and strain tensors; in such cases we refer to "gradient elasticity" theories. Mindlin [14] presented several alternative *equivalent* formulations of his theory by using different kinematic variables in the elastic strain energy density function W.

In the present study we focus on mode-I cracks and apply the formulation of strain-gradient elasticity developed by Mindlin and co-workers (Mindlin [14], Mindlin and Eshel [16]). Chapter 2 gives a description of the aforementioned formulation where W is written in terms of the strain, the spatial gradient of rotation, and the fully symmetric part of the second spatial gradient of displacement (or of the gradient of strain). The variational formulation developed by Amanatidou and Aravas [1] is described thoroughly in Chapter 3. In the latter case since "Type III" form is used, the calculation of the true stress σ and the true couple stress μ is straightforward. In Chapters 4 and 5 we consider the plane strain problem of a center-cracked panel (CCP) and an edge-cracked panel (ECP) respectively. The specimens and the applied loads are symmetric with respect to the crack plane (mode-I) in both cases. We carry out detailed finite element calculations and we proceed comparing the results with the asymptotic solutions developed by Aravas and Giannakopoulos [2] where the singular $(1/\sqrt{r})$ strains in the classical solution $(\ell = 0)$ have been replaced by the finite (asymptotically constant) strains of the gradient elasticity solution $(\ell > 0)$ at the crack-tip.

Chapter 2

Mindlin Type III strain-gradient elasticity theory

2.1 Notation and conventions

2.1.1 Tensor products

Standard notation is used throughout. Boldface symbols denote tensors the orders of which are indicated by the context. All tensor components are written with respect to a fixed Cartesian coordinate system with base vectors $\mathbf{e}_i$ $(i = 1, 2, 3)$, and the summation convention is used for repeated Latin indices, unless otherwise indicated. The prefixes "tr" and "det" indicate the trace and the determinant respectively, a superscript T the transpose of a second order tensor, and the subscripts S and A the symmetric and anti-symmetric parts of a second order tensor. Let $(\mathbf{a},\mathbf{b})$ be vectors, and $(\mathbf{A},\mathbf{B})$ second order tensors; the following products are used in the text $\mathbf{a} \cdot \mathbf{b} = a_i\,b_i$, $(\mathbf{ab})_{ij} = a_i\,b_j$, $(\mathbf{a} \cdot \mathbf{A})_i = a_k\,A_{ki}$, $(\mathbf{A} \cdot \mathbf{a})_i = A_{ik}\,a_k$, $(\mathbf{A} \cdot \mathbf{B})_{ij} = A_{ik}\,B_{kj}$, and $\mathbf{A} : \mathbf{B} = A_{ij}\,B_{ij}$. A comma followed by a subscript, say i, denotes partial differentiation with respect to the spatial coordinate x_i, i.e., $A_{,i} = \partial A/\partial x_i$. The following notation is also used for the symmetric and antisymmentric parts of a second order tensor:

$$A_{ij}^S = A_{(ij)} \equiv \frac{1}{2}(A_{ij} + A_{ji}), \qquad A_{ij}^A = A_{[ij]} \equiv \frac{1}{2}(A_{ij} - A_{ji}). \qquad (2.1)$$

2.1.2 "Normal" and "tangential" parts of tensors

Let S be the bounding surface of a body and $\mathbf{n}$ the outward unit normal to S. We consider a vector field $\mathbf{a}$ defined on S and define its "normal" $(\mathbf{a}^n)$ and "tangetial" $(\mathbf{a}^t)$ parts as

$$\mathbf{a}^n = (\mathbf{a} \cdot \mathbf{n})\,\mathbf{n} \qquad \text{and} \qquad \mathbf{a}^t = \mathbf{a} - \mathbf{a}^n. \qquad (2.2)$$

Similarly, if $\mathbf{A}$ is a second-order tensor field $\mathbf{A}$ on S, we define its "normal" $(\mathbf{A}^n)$ and "tangetial" $(\mathbf{A}^t)$ parts as

$$\mathbf{A}^n = (\mathbf{A} \cdot \mathbf{n})\,\mathbf{n} = \mathbf{A} \cdot (\mathbf{n}\,\mathbf{n}) \qquad \text{and} \qquad \mathbf{A}^t = \mathbf{A} - \mathbf{A}^n. \qquad (2.3)$$

If **A** and **B** are second-order tensors, it can be shown easily that

$$\mathbf{A}^n : \mathbf{B}^t = \mathbf{A}^t : \mathbf{B}^n = 0, \qquad \mathbf{A} : \mathbf{B} = \mathbf{A}^n : \mathbf{B}^n + \mathbf{A}^t : \mathbf{B}^t \qquad \text{and} \qquad \mathbf{A}^t \cdot \mathbf{n} = \mathbf{0}. \tag{2.4}$$

On S we define also the normal derivative D of a field f as the normal component of $\nabla f = f_{,i}\,\mathbf{e}_i$, i.e.,

$$Df = (\nabla f) \cdot \mathbf{n} = f_{,i}\,n_i. \tag{2.5}$$

The "surface gradient" $\mathbf{D}f$ on S is defined as the tangential part of ∇f, i.e.,

$$\mathbf{D}f = \nabla f - (Df)\,\mathbf{n} \qquad \text{or} \qquad D_i f = f_{,i} - f_{,k}\,n_k\,n_i. \tag{2.6}$$

It should be noted that the tangential derivative of the unit vector $\mathbf{n}$ normal to the bounding surface S obeys the law[1]

$$D_j n_i = D_i n_j. \tag{2.7}$$

If we consider the second order tensor, say $\mathbf{A}$, defined by the gradient of a vector field $\mathbf{u}$ on S, i.e.,

$$\mathbf{A} = \mathbf{u}\nabla \qquad \text{or} \qquad A_{ij} = u_{i,j}, \tag{2.8}$$

then it can be shown easily that

$$\mathbf{A}^n = (D\mathbf{u})\,\mathbf{n} \qquad \text{and} \qquad \mathbf{A}^t = \mathbf{u}\mathbf{D} \tag{2.9}$$

or

$$A_{ij}^n = (Du_i)\,n_j \qquad \text{and} \qquad A_{ij}^t = D_j u_i, \tag{2.10}$$

i.e., $\mathbf{A}^n$ consists of the derivatives of the components u_i in the direction normal to S, whereas $\mathbf{A}^t$ contains the derivatives of u_i on a plane tangent to S.

Amanatidou and Aravas [1] have shown that for every second order tensor $\mathbf{A}$

$$A_{ij}^n = n_k\,A_{ki}^t\,n_j + 2\,A_{[ik]}\,n_k\,n_j + n_k\,A_{(kp)}\,n_p\,n_i\,n_j. \tag{2.11}$$

If we set now $A_{ij} = u_{i,j}$ in the last equation, we find that

$$(Du_i)\,n_j = n_k\,n_j\,D_i u_k + 2\,u_{[i,k]}\,n_k\,n_j + n_k\,u_{(k,p)}\,n_p\,n_i\,n_j. \tag{2.12}$$

---

[1] The proof (2.7) is based on the fact that $\mathbf{n}$ can be written in the form $\mathbf{n} = \nabla F/|\nabla F|$, where $F(\mathbf{x}) = 0$ is the function that defines analytically the surface S. It can be shown readily that the quantity $D_j n_i = n_{i,j} - n_{i,k}\,n_k\,n_j$ is symmetric with reepect to i and j.

2.2 Kinematic variables

Let $\boldsymbol{u}$ be the displacement field. The following quantities are defined:

$$\epsilon_{ij} = u_{(i,j)} = \frac{1}{2}\left(u_{i,j} + u_{j,i}\right) = \text{infinitesimal strain,} \tag{2.13}$$

$$\Omega_{ij} = u_{[i,j]} = \frac{1}{2}\left(u_{i,j} - u_{j,i}\right) = -e_{ijk}\,\omega_k = \text{infinitesimal rotation tensor,} \tag{2.14}$$

$$\omega_i = \frac{1}{2}\left(\nabla \times \boldsymbol{u}\right)_i = \frac{1}{2}\,e_{ijk}\,u_{k,j} = -\frac{1}{2}\,e_{ijk}\,\Omega_{jk} = \text{infinitesimal rotation vector,} \tag{2.15}$$

$$\bar{\kappa}_{ij} = \omega_{j,i} = \text{infinitesimal rotation gradient,} \qquad \bar{\kappa}_{ii} = 0, \tag{2.16}$$

$$\bar{\bar{\kappa}}_{ijk} = \frac{1}{3}\left(u_{i,jk} + u_{j,ki} + u_{k,ij}\right) = \frac{1}{3}\left(\epsilon_{ij,k} + \epsilon_{jk,i} + \epsilon_{ki,j}\right) = \bar{\bar{\kappa}}_{jik} = \bar{\bar{\kappa}}_{ikj} = \bar{\bar{\kappa}}_{kji}, \tag{2.17}$$

where e_{ijk} is the alternating symbol.

2.3 Constitutive equations

The strain energy density W is written in the form:

$$W = \bar{W}(\boldsymbol{\epsilon}, \bar{\boldsymbol{\kappa}}, \bar{\bar{\boldsymbol{\kappa}}}). \tag{2.18}$$

Mindlin refers to the description $W = \bar{W}(\boldsymbol{\epsilon}, \bar{\boldsymbol{\kappa}}, \bar{\bar{\boldsymbol{\kappa}}})$ as "**Type III**". Mindlin and Eshel [16] present the most general form of $\bar{W}$ for an isotropic linear elastic material. Using the above form of the elastic strain energy density, one defines the following quantities:

$$\bar{\sigma}_{ij} = \frac{\partial \bar{W}}{\partial \epsilon_{ij}} = \bar{\sigma}_{ji}, \tag{2.19}$$

$$\bar{\mu}_{ij} = \frac{\partial \bar{W}}{\partial \bar{\kappa}_{ij}}, \qquad \bar{\bar{\mu}}_{ijk} = \frac{\partial \bar{W}}{\partial \bar{\bar{\kappa}}_{ijk}} = \bar{\bar{\mu}}_{jik} = \bar{\bar{\mu}}_{ikj} = \bar{\bar{\mu}}_{kji}. \tag{2.20}$$

It is worthy of note that $\bar{\sigma}_{ij}$, $\bar{\mu}_{ij}$, and $\bar{\bar{\mu}}_{ijk}$ are introduced as "conjugate" quantities to ϵ_{ij}, $\bar{\kappa}_{ij}$ and $\bar{\bar{\kappa}}_{ijk}$, and their relationship to "true" stress or "true" couple stress is not obvious; this relationship is discussed in Section 2.5. It should be noted also that the so-called "micropolar theory of elasticity" (Toupin [19], Koiter [10][11], Mindlin and Tiersten [17]) is a special case of the above theory. In fact, if $\bar{W}$ is independent of $\bar{\bar{\kappa}}_{ijk}$, i.e. $W = \bar{W}(\epsilon_{ij}, \bar{\kappa}_{ij})$, then $\bar{\bar{\mu}}_{ijk} \equiv 0$ and $\bar{\mu}_{ij}$ becomes the usual "couple stress" tensor. The variation of the internal work is given in a separate expression for form III of W:

$$\delta W^{int} = \int\limits_V \delta W\, dV = \int\limits_V \left(\bar{\sigma}_{ij}\,\delta\epsilon_{ij} + \bar{\mu}_{ij}\,\delta\bar{\kappa}_{ij} + \bar{\bar{\mu}}_{ijk}\,\bar{\bar{\kappa}}_{ijk}\right)\, dV, \tag{2.21}$$

where V is the volume of the elastic body. Let f_i be the "body force" per unit volume and Φ_{ij} the "body double force" per unit volume. Using equation(2.21) and making use of Stokes' surface divergence theory, we adopt the following form for the variation of work done

by external forces for form III of W (Mindlin [14], Mindlin and Eshel [16]):

$$
\begin{aligned}
\delta W^{ext} &= \int_V \left(f_i\,\delta u_i + \Phi_{[ij]}\,\delta\Omega_{ji} + \Phi_{(ij)}\,\delta\epsilon_{ji} \right)\,dV + \int_S \left(\bar{P}_i\,\delta u_i + \bar{Q}_i^t\,\delta\omega_i^t + \bar{R}\,\delta\epsilon^n \right)\,dV + \\
&\quad + \sum_\alpha \oint_{C^\alpha} \bar{E}_i\,\delta u_i\,ds,
\end{aligned}
\tag{2.22}
$$

where S is the bounding surface of the elastic body, $\epsilon^n = n_i\,\epsilon_{ij}\,n_j = \mathbf{n}\cdot\boldsymbol{\epsilon}\cdot\mathbf{n}$ the component of the strain tensor in the direction normal to S, and $(\bar{\mathbf{P}}, \bar{\mathbf{Q}}^t, \bar{R}, \bar{\mathbf{E}})$ are generalized external forces, which are defined precisely in the following. In the above equation, the line integrals over C^α are included when the outer surface S is piecewise smooth; in such a case, the surface S can be divided into a finite number of smooth surfaces S^α ($\alpha = 1, 2, \dots$) each bounded by an edge C^α, and integration is conducted along the arc length of each C^α. We note that the body moment per unit volume is $M_i = e_{ijk}\,\Phi_{[jk]}$ (or $\Phi_{ij} = \frac{1}{2}\,e_{ijk}\,M_k$), so that the term $\Phi_{[ij]}\,\delta\Omega_{ji}$ in (2.22) can be written also as $\Phi_{[ij]}\,\delta\Omega_{ji} = M_i\,\delta\omega_i$, where $\delta\omega_i = -\frac{1}{2}\,e_{ijk}\,\delta\Omega_{jk}$. The identity $\delta W^{int} = \delta W^{ext}$ leads to the following relations for the "external forces" ([14][16]):

Type III

$$
\bar{P}_i = n_j \left(\bar{\sigma}_{ji} - \frac{1}{2}\,\bar{\mu}_{pk,p}\,e_{jik} - \bar{\bar{\mu}}_{kji,k} - \Phi_{ji} \right) - \frac{1}{2}\,n_j\,\bar{\mu}_{,k}^n\,e_{ijk} -
$$
$$
- [D_j - (D_p n_p)\,n_j](n_k\,\bar{\bar{\mu}}_{kji} + n_i\,n_q\,n_p\,\bar{\bar{\mu}}_{pqj}),
\tag{2.23}
$$

$$
\bar{Q}_i^t = n_j\,\bar{\mu}_{ji}^t + 2\,n_q\,n_j\,n_k\,\bar{\bar{\mu}}_{kjp}\,e_{qpi},
\tag{2.24}
$$

$$
\bar{R} = n_i\,n_j\,n_k\,\bar{\bar{\mu}}_{ijk},
\tag{2.25}
$$

$$
\bar{E}_i = [[\frac{1}{2}s_i\,\bar{\mu}^n + \ell_j\,n_k\,(\bar{\bar{\mu}}_{kji} + n_i\,n_p\,\bar{\bar{\mu}}_{pkj}]],
\tag{2.26}
$$

where $\bar{\mu}^n = n_i\,\bar{\mu}_{ij}\,n_j = \mathbf{n}\cdot\bar{\boldsymbol{\mu}}\cdot\mathbf{n}$ on S.

In the above expressions, the double brackets $[[\ \ ]]$ indicate the jump in the value of the enclosed quantity across C^α, and $\boldsymbol{\ell} = \mathbf{s}\times\mathbf{n}$, where $\mathbf{s}$ is the unit vector tangent to C^α.

2.4   Boundary value problem

Mindlin and Eshel [16] have shown that the equilibrium equations and the appropriate boundary conditions for Type III formulation are as follows:

Type III

$$
(\bar{\sigma}_{ji} - \bar{\bar{\mu}}_{kji,k} - \frac{1}{2}\,\bar{\mu}_{pk,p}\,e_{jik} - \Phi_{ji})_{,j} + f_i = 0 \qquad \text{in} \ \ V.
\tag{2.27}
$$

At each point on the boundary S the following are specified: i) u_i or $\bar{P}_i$, ii) ω_i^t or $\bar{Q}_i^t$, and iii) ϵ^n or $\bar{R}$. If S is piecewise smooth, then u_i or $\bar{E}_i$ is also specified at each point on the edges C^α.

2.5 Relation to true stress, true couple-stress and true loads

In this section we discuss the relationship between $\bar{\sigma}_{ij}$, $\bar{\mu}_{ij}$, $\bar{\bar{\mu}}_{ijk}$ defined in Section 2.3 and the "true" stresses. Also the relations between the "external loads" $\bar{P}_i$, $\bar{Q}_i^t$, $\bar{R}$, $\bar{E}_i$ and the "true" loads are discussed. Let σ_{ij} be the usual true stress tensor and μ_{ij} the couple-stress tensor. On an infinitesimal area with unit normal vector $\mathbf{n}$, the traction vector $\mathbf{t}$ and the couple vector $\mathbf{m}$ are related to $\boldsymbol{\sigma}$ and $\boldsymbol{\mu}$ by

$$t_i = n_j\,\sigma_{ji} \qquad \text{and} \qquad m_i = n_j\,\mu_{ji}. \tag{2.28}$$

If the body force per unit volume is f_i and the body moment per unit volume is $M_i = e_{ijk}\,\Phi_{[jk]}$, then the principles of linear and angular momentum lead to the well known equations

$$\sigma_{ji,j} + f_i = 0 \qquad \text{and} \qquad \sigma_{[ij]} + \frac{1}{2}\,\mu_{pk,p}\,e_{ijk} + \Phi_{[ij]} = 0. \tag{2.29}$$

Mindlin and Eshel [16] adopt the following expression for the variation of the work done by external forces:

$$\delta W^{ext} = \int\limits_V \left(f_i\,\delta u_i + \Phi_{[ij]}\,\delta\Omega_{ji} + \Phi_{(ij)}\,\delta\epsilon_{ji} \right) dV + \int\limits_S \left(t_i\,\delta u_i + m_i\,\delta\omega_i + n_i\,\bar{\bar{\mu}}_{ijk}\,\delta\epsilon_{jk} \right) dV +$$

$$+ \sum_\alpha \oint\limits_{C^\alpha} \bar{E}_i\,\delta u_i\,ds. \tag{2.30}$$

It should be noted that the last two terms in each of the integrals of (2.30) can be written as

$$\Phi_{[ij]}\,\delta\Omega_{ji} + \Phi_{(ij)}\,\delta\epsilon_{ji} = \Phi_{ij}\,\delta u_{j,i}, \tag{2.31}$$

and

$$m_i\,\delta\omega_i + n_i\,\bar{\bar{\mu}}_{ijk}\,\delta\epsilon_{jk} = T_{[ij]}\,\delta\Omega_{ji} + T_{(ij)}\,\delta\epsilon_{ji} = T_{ij}\,\delta u_{j,i}, \tag{2.32}$$

where $\boldsymbol{\Phi}$ is the "body double force" per unit volume, and $\boldsymbol{T}$ the "surface double force" per unit area (or "double traction") defined on S as

$$T_{ij}^S \equiv T_{(ij)} = n_k\,\bar{\bar{\mu}}_{kij} \qquad \text{and} \qquad T_{ij}^A \equiv T_{[ij]} = \frac{1}{2}\,e_{ijk}\,m_k = \frac{1}{2}\,e_{ijk}\,n_p\,\mu_{pk}. \tag{2.33}$$

Using the above expression for δW^{ext}, and setting it equal to

$$\delta W^{int} = \int\limits_V \left(\bar{\sigma}_{ij}\,\delta\epsilon_{ij} + \bar{\mu}_{ij}\,\delta\bar{\kappa}_{ij} + \bar{\bar{\mu}}_{ijk}\,\delta\bar{\bar{\kappa}}_{ijk} \right) dV. \tag{2.34}$$

Mindlin and Eshel [16] have shown that the true stress $\boldsymbol{\sigma}$ is related to $\bar{\boldsymbol{\sigma}}$, $\bar{\boldsymbol{\mu}}$ and $\bar{\bar{\boldsymbol{\mu}}}$ by the expressions

$$\sigma_{(ij)} = \bar{\sigma}_{ij} - \bar{\bar{\mu}}_{ijk,k} - \Phi_{(ij)}, \tag{2.35}$$

$$\sigma_{[ij]} = -\frac{1}{2}\,e_{ijk}\,\bar{\mu}_{pk,p} - \Phi_{[ij]}, \tag{2.36}$$

and the true couple stress $\boldsymbol{\mu}$ is[2]

$$\mu_{ij} = \bar{\mu}_{ij}. \tag{2.38}$$

In view of the last equation the surface double force $\boldsymbol{T}$ can be written as

$$T_{ij} = n_k\,\bar{\bar{\mu}}_{kij} + \frac{1}{2}\,e_{ijk}\,n_p\,\bar{\mu}_{pk}. \tag{2.39}$$

Using the definition of $\bar{P}_i$, $\bar{Q}_i^t$, $\bar{R}$ and $\bar{E}_i$ given in (2.23)–(2.26) and equations (2.35)–(2.38) above, we can show easily that the "mathematical" loads $(\bar{P}_i, \bar{Q}_i^t, \bar{R}, \bar{E}_i)$ are related to the true loads $(t_i, m_i, T_{(ij)})$ by the following expressions:

$$\bar{P}_i = t_i - \frac{1}{2}\,e_{ijk}\,D_k(m_p\,n_p\,n_j) + [(D_p n_p)\,n_j - D_j]\,(T_{(ji)} + n_k\,T_{(kj)}\,n_i), \tag{2.40}$$

$$\bar{Q}_i^t = m_i^t + 2\,e_{qpi}\,n_q\,n_j\,T_{(pj)}, \tag{2.41}$$

$$\bar{R} = n_i\,T_{(ij)}\,n_j, \tag{2.42}$$

$$\bar{E}_i = [[\frac{1}{2}\,s_i\,m_j\,n_j + \ell_j\,(T_{(ij)} + n_i\,T_{(jk)}\,n_k)]]. \tag{2.43}$$

Using direct notation, we can write the above relationships in the form

$$\bar{\mathbf{P}} = \mathbf{t} + \frac{1}{2}\,\mathbf{D} \times [(\mathbf{m} \cdot \mathbf{n})\,\mathbf{n}] + [(\mathbf{D} \cdot \mathbf{n})\,\mathbf{n} - \mathbf{D}] \cdot (\mathbf{T}^S + \mathbf{n} \cdot \mathbf{T}^S\,\mathbf{n}) \tag{2.44}$$

$$\bar{\mathbf{Q}}^t = \mathbf{m}^t + 2\,\mathbf{n} \times (\mathbf{n} \cdot \mathbf{T}^S), \tag{2.45}$$

$$\bar{R} = \mathbf{n} \cdot \mathbf{T}^S \cdot \mathbf{n}, \tag{2.46}$$

$$\bar{\mathbf{E}} = [[\frac{1}{2}\,(\mathbf{m} \cdot \mathbf{n})\,\mathbf{s} + \boldsymbol{\ell} \cdot \mathbf{T}^S \cdot (\mathbf{I} + \mathbf{n}\,\mathbf{n})]]. \tag{2.47}$$

The relationship between "true" and "mathematical" stresses and loads is discussed also by Germain in [7] and [9], where "higher order" volumetric forces are also considered. It should be noted that in physical problems one would, presumably, have information about the body force f_i and the body double force Φ_{ij} throughout the volume V, and the true traction t_i, the true moment per unit area m_i, and the double traction $T_{(ij)}$ on the surface S. Equations (2.40)–(2.47) indicate the way in which this information is to be employed in setting up the boundary "loads" in Type III boundary value problems discussed in Section 2.4 within the framework of strain-gradient elasticity. It should be noted though that the true loads $(t_i, m_i, T_{(ij)})$ cannot be prescribed directly; instead, they enter the boundary conditions in certain combinations according to (2.40)–(2.47). Finally, after the boundary value problem of Section 2.4 has been solved, the true stresses σ_{ij} and true couple-stresses μ_{ij} are determined from equations (2.35)–(2.38).

---

[2] Note that micropolar theory of elasticity $\bar{\bar{\mu}}_{ijk} = 0$, so that

$$\sigma_{(ij)} = \bar{\sigma}_{ij} - \Phi_{(ij)}, \qquad \sigma_{[ij]} = -\frac{1}{2}\,e_{ijk}\,\bar{\mu}_{pk,p} - \Phi_{[ij]}, \qquad \text{and} \qquad \mu_{ij} = \bar{\mu}_{ij}. \tag{2.37}$$

Chapter 3

Variational formulation

Here we discuss the Type III formulation and emphasize the calculation of true stresses and true couple stresses.

3.1   Type III formulation

The governing equations in V are ($\boldsymbol{\Phi} = \mathbf{0}$):

$$\sigma_{ji,j} + f_i = 0, \tag{3.1}$$

$$\sigma_{ij} = \bar{\sigma}_{ij} + \bar{\sigma}_{ij}^{(2)}, \qquad \bar{\sigma}_{ij}^{(2)} = -\bar{\bar{\mu}}_{kij,k} - \frac{1}{2}\, e_{ijk}\, \bar{\mu}_{pk,p}, \tag{3.2}$$

$$\epsilon_{ij} = u_{(i,j)}, \qquad \omega_i = -\frac{1}{2}\, e_{ijk}\, u_{j,k} \qquad \text{or} \qquad u_{[i,j]} = -e_{ijk}\, \omega_k, \tag{3.3}$$

$$\bar{\kappa}_{ij} = \omega_{j,i}, \qquad \bar{\bar{\kappa}}_{ijk} = \frac{1}{3}\,(\epsilon_{ij,k} + \epsilon_{jk,i} + \epsilon_{ki,j}), \tag{3.4}$$

$$\bar{\sigma}_{ij} = \frac{\partial \bar{W}}{\partial \epsilon_{ij}}, \qquad \bar{\mu}_{ij} = \frac{\partial \bar{W}}{\partial \bar{\kappa}_{ij}}, \qquad \bar{\bar{\mu}}_{ijk} = \frac{\partial \bar{W}}{\partial \bar{\bar{\kappa}}_{ijk}}. \tag{3.5}$$

The corresponding boundary conditions are

$$u_i = \bar{u}_i \quad \text{on} \;\; S_u, \tag{3.6}$$

$$n_j\, \sigma_{ji} - \frac{1}{2}\, n_j\, \bar{\mu}_{,k}^n\, e_{ijk} + [(D_p n_p)\, n_j - D_j](n_k\, \bar{\bar{\mu}}_{kji} + n_i\, n_p\, n_k\, \bar{\bar{\mu}}_{kpj}) = \bar{P}_i \quad \text{on} \;\; S_P, \tag{3.7}$$

$$\omega_i^t = \bar{\omega}_i^t \quad \text{on} \;\; S_\omega, \tag{3.8}$$

$$n_j\, \bar{\mu}_{ji}^t + 2\, n_q\, n_j\, n_k\, \bar{\bar{\mu}}_{kjp}\, e_{qpi} = \bar{Q}_i^t \quad \text{on} \;\; S_Q, \tag{3.9}$$

$$n_i\, n_j\, \epsilon_{ij} = \bar{\epsilon} \quad \text{on} \;\; S_\epsilon, \tag{3.10}$$

$$n_i\, n_j\, n_k\, \bar{\bar{\mu}}_{ijk} = \bar{R} \quad \text{on} \;\; S_R, \tag{3.11}$$

$$u_i = \bar{u}_i^\alpha \quad \text{on} \;\; C_u^\alpha, \tag{3.12}$$

$$[[\frac{1}{2} s_i\, \bar{\mu}^n + \ell_j\, n_k\, (\bar{\bar{\mu}}_{kji} + n_i\, n_p\, \bar{\bar{\mu}}_{pjk})]] = \bar{E}_i^\alpha \quad \text{on} \;\; C_E^\alpha, \tag{3.13}$$

where $\bar{\mu}^n = n_i\, n_j\, \bar{\mu}_{ij}$, $(\bar{\mathbf{u}}, \bar{\mathbf{P}}, \bar{\boldsymbol{\omega}}^t, \bar{\mathbf{Q}}^t, \bar{\epsilon}, \bar{R}, \bar{\mathbf{u}}^\alpha, \bar{\mathbf{E}}^\alpha)$ are known functions, $S_u \cup S_P = S_\omega \cup S_Q = S_\epsilon \cup S_R = S$, $S_u \cap S_P = S_\omega \cap S_Q = S_\epsilon \cap S_R = \emptyset$, $C_u^\alpha \cup C_E^\alpha = C^\alpha$ and $C_u^\alpha \cap C_E^\alpha = \emptyset$.

We recall that, if we omit the terms involving $\bar{\bar{\kappa}}$ in $\bar{W}$, set $\bar{\bar{\mu}} = \mathbf{0}$ and $S_\epsilon = S_R = \emptyset$, then we recover the standard boundary value problem of "micropolar elasticity" (Toupin [19], Koiter [10][11], Mindlin and Tiersten [17]).

Amanatidou and Aravas [1] presented a variational formulation of the problem, in which $\mathbf{u}$, $\boldsymbol{\omega}$, $\boldsymbol{\epsilon}$ and $\boldsymbol{\sigma}^{(2)}$ were viewed as the primary unknowns. In particular, the quantities $\mathbf{u}$, $\boldsymbol{\omega}$ and $\boldsymbol{\epsilon}$ were considered as independent variables subject to suitable side conditions. These side conditions were:

i) the kinematical equations $u_{i,j} = \epsilon_{ij} - e_{ijk}\,\omega_k$ in the entire body, and

ii) the expression of the tangential part of the $\epsilon_{ij} - e_{ijk}\,\omega_k$ on the entire surface S in terms of the tangential derivatives $D_j u_i$ of the displacement, i.e.,

$$D_j u_i = (\epsilon_{ij} - e_{ijk}\,\omega_k)^t = \epsilon_{ij} - e_{ijk}\,\omega_k - \epsilon_{ik}\,n_k\,n_j + e_{ipk}\,\omega_k\,n_p\,n_j \quad \text{on } S. \qquad (3.14)$$

Amanatidou and Aravas [1] showed that the solution to the problem can be given also by the stationarity condition $\delta\Pi = 0$ of the functional

$$\Pi(\mathbf{u}, \boldsymbol{\omega}, \boldsymbol{\epsilon}, \bar{\boldsymbol{\sigma}}^{(2)}) = \int_V \bar{W}(u_{(i,j)}, \bar{\boldsymbol{\kappa}}(\boldsymbol{\omega}), \bar{\bar{\boldsymbol{\kappa}}}(\boldsymbol{\epsilon}))\,dV + \int_V [u_{i,j} - (\epsilon_{ij} - e_{ijk}\,\omega_k)]\,\bar{\sigma}_{ji}^{(2)}\,dV - $$

$$- \int_V f_i\,u_i\,dV - \int_{S_P} \bar{P}_i\,u_i\,dS - \int_{S_Q} \bar{Q}_i^t\,\omega_i^t\,dS - \int_{S_R} \bar{R}\,n_i\,n_j\,\epsilon_{ij}\,dS - \sum_\alpha \oint_{C_E^\alpha} \bar{E}_i^\alpha\,u_i\,ds + $$

$$+ \int_S [u_{(i,j)} - 2\,n_j\,n_k\,u_{[i,k]} - n_i\,n_j\,n_p\,n_q\,u_{(p,q)} - $$

$$- (\epsilon_{ij} + 2\,n_j\,n_k\,e_{ikp}\,\omega_p - n_i\,n_j\,n_p\,n_q\,\epsilon_{pq})]\,n_r\,\bar{\bar{\mu}}_{rij}\,dS + $$

$$+ \int_S \left(\frac{1}{2}\,e_{ijk}\,u_{k,j}\,n_i - \omega_i\,n_i\right)\,n_p\,\bar{\mu}_{pq}\,n_q\,dS, \qquad (3.15)$$

where $\epsilon_{ji} = \epsilon_{ij}$, $\bar{\kappa}_{ij}(\boldsymbol{\omega}) = \omega_{j,i}$, $\bar{\bar{\kappa}}_{ijk}(\boldsymbol{\epsilon}) = (1/3)\,(\epsilon_{ij,k} + \epsilon_{jk,i} + \epsilon_{ki,j})$, $\bar{W} = \bar{W}(u_{(i,j)}, \bar{\boldsymbol{\kappa}}(\boldsymbol{\omega}), \bar{\bar{\boldsymbol{\kappa}}}(\boldsymbol{\epsilon}))$, $\bar{\mu}_{ij}(\mathbf{u}, \boldsymbol{\omega}, \boldsymbol{\epsilon}) = \partial\bar{W}/\partial\bar{\kappa}_{ij}$, $\bar{\bar{\mu}}_{ijk}(\mathbf{u}, \boldsymbol{\omega}, \boldsymbol{\epsilon}) = \partial\bar{W}/\partial\bar{\bar{\kappa}}_{ijk}$, $\delta\mathbf{u} = \mathbf{0}$ on S_u and C_u^α, $\delta\boldsymbol{\omega}^t = \mathbf{0}$ on S_ω, and $\mathbf{n} \cdot \delta\boldsymbol{\varepsilon} \cdot \mathbf{n} = 0$ on S_ϵ. The stationarity condition $\delta\Pi = 0$ implies the appropriate field equations and boundary conditions, $\bar{\sigma}_{ij}^{(2)} = -\bar{\bar{\mu}}_{kij,k} - (1/2)\,e_{ijk}\,\bar{\mu}_{pk,p}$ in V, and $D_j u_i = (\epsilon_{ij} - e_{ijk}\,\omega_k)^t$ on S.

In the two dimensional case, the last term in the above functional vanishes identicaly and the integrals over C_E^α are replaced by

$$\sum_\alpha \bar{E}_i^\alpha\,u_i, \qquad (3.16)$$

where the sum over α refers to any corners that may exist on the bounding curve of the two-dimensional body.

Chapter 4

The Center Cracked Panel (CCP) — Finite Element Plane Strain Solutions

4.1 Finite element formulation

In the examples that follow, we consider a material with an elastic strain energy density of the form

$$W = \bar{W}(\boldsymbol{\epsilon}, \bar{\boldsymbol{\kappa}}, \bar{\bar{\boldsymbol{\kappa}}}), \tag{4.1}$$

where

$$\bar{W}(\boldsymbol{\epsilon}, \bar{\boldsymbol{\kappa}}, \bar{\bar{\boldsymbol{\kappa}}}) = \frac{1}{2}\,\lambda\,\epsilon_{ii}\,\epsilon_{kk} + \mu\,\epsilon_{ij}\,\epsilon_{ij} + \ell^2\left[\frac{2}{9}\,(\lambda + 3\,\mu)\,\bar{\kappa}_{ij}\,\bar{\kappa}_{ij} - \frac{2}{9}\,\lambda\,\bar{\kappa}_{ij}\,\bar{\kappa}_{ji} + \right.$$
$$\left. + \frac{1}{2}\,\lambda\,\bar{\bar{\kappa}}_{iij}\,\bar{\bar{\kappa}}_{kkj} + \mu\,\bar{\bar{\kappa}}_{ijk}\,\bar{\bar{\kappa}}_{ijk} + \frac{2}{3}\,\lambda\,e_{ijk}\,\bar{\kappa}_{ij}\,\bar{\bar{\kappa}}_{kpp}\right], \tag{4.2}$$

so that

$$\bar{\sigma}_{ij} = \frac{\partial \bar{W}}{\partial \epsilon_{ij}} = 2\,\mu\,\epsilon_{ij} + \lambda\,\epsilon_{kk}\,\delta_{ij}, \tag{4.3}$$

$$\bar{\mu}_{ij} = \frac{\partial \bar{W}}{\partial \bar{\kappa}_{ij}} = \frac{2\,\ell^2}{9}\left[2\,(\lambda + 3\,\mu)\,\bar{\kappa}_{ij} - 2\,\lambda\,\bar{\kappa}_{ji} + 3\,\lambda\,e_{ijk}\,\bar{\bar{\kappa}}_{kpp}\right], \tag{4.4}$$

$$\bar{\bar{\mu}}_{ijk} = \frac{\partial \bar{W}}{\partial \bar{\bar{\kappa}}_{ijk}} = \frac{\ell^2}{9}\left[3\,\lambda\,(\bar{\bar{\kappa}}_{ppk}\,\delta_{ij} + \bar{\bar{\kappa}}_{ppi}\,\delta_{jk} + \bar{\bar{\kappa}}_{ppj}\,\delta_{ki}) + 18\,\mu\bar{\bar{\kappa}}_{ijk} + \right.$$
$$\left. + 2\,\lambda\,\bar{\kappa}_{pq}\,(\delta_{ij}\,e_{pqk} + \delta_{jk}\,e_{pqi} + \delta_{ki}\,e_{pqj})\right]. \tag{4.5}$$

In the above equations, μ and λ are the usual Lamé constants and ℓ is a material length scale. For the gradient model presented above, several boundary value problems have been solved analytically (e.g., Georgiadis [6], Exadaktylos [4]).

In the following, the center-cracked panel problem is solved by using the variational formulation presented in Section 3.1 together with the finite element method and the obtained numerical solutions are compared to the corresponding asymptotic solutions developed by Aravas and Giannakopoulos [2]. The finite element formulation is "mixed" [21] and independent interpolations for $\mathbf{u}$, $\boldsymbol{\omega}$, $\boldsymbol{\epsilon}$ and $\boldsymbol{\sigma}^{(2)}$ are used. In particular, the nine-node plane-strain isoparametric element with 70 degrees of freedom developed by Amanatidou and Aravas [1]
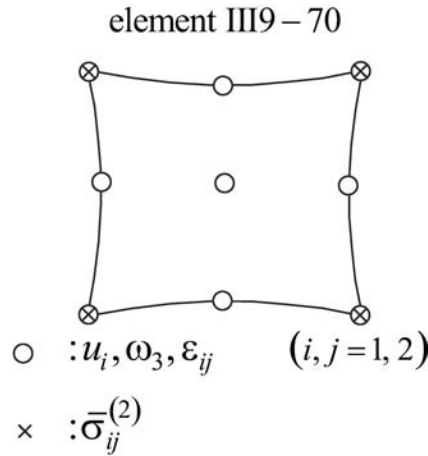
element III9 − 70

Figure 4.1: Nine-node finite element and the corresponding degrees of freedom.

is used (III9-70 in [1]). The quantities $(u_1, u_2, \omega_3, \epsilon_{11}, \epsilon_{22}, 2\epsilon_{12})$ are used as degrees of freedom at all nodes; the quantities $(\bar{\sigma}_{11}^{(2)}, \bar{\sigma}_{22}^{(2)}, \bar{\sigma}_{(12)}^{(2)}, \bar{\sigma}_{[12]}^{(2)})$ are additional degrees of freedom at the corner nodes (Fig. 4.1). A bi-quadratic Lagrangian interpolation for $(u_1, u_2, \omega_3, \epsilon_{11}, \epsilon_{22}, 2\epsilon_{12})$ and a bi-linear interpolation for $(\bar{\sigma}_{11}^{(2)}, \bar{\sigma}_{22}^{(2)}, \bar{\sigma}_{(12)}^{(2)}, \bar{\sigma}_{[12]}^{(2)})$ are used in the isoparametric plane. The resulting global interpolation for all nodal quantities is now continuous in a finite element mesh.

This element was implemented in the ABAQUS general purpose finite element program. This code provides a general interface so that a particular finite element can be introduced as a user subroutine (UEL).

4.2   The center cracked panel (CCP)

In order to verify the asymptotic crack-tip solution (Aravas and Giannakopoulos [2]) and determine its region of dominance, we carry out detailed finite element calculations of a cracked specimen under mode-I plane-strain conditions. We consider the center-cracked panel (CCP) subjected to uniaxial tension σ^∞ as shown in Fig. 4.2.

Both the specimen and the applied loads are symmetric with respect to the crack plane (mode-I). Because of symmetry, one quarter of the specimen is analyzed (Fig. 4.3a) and the
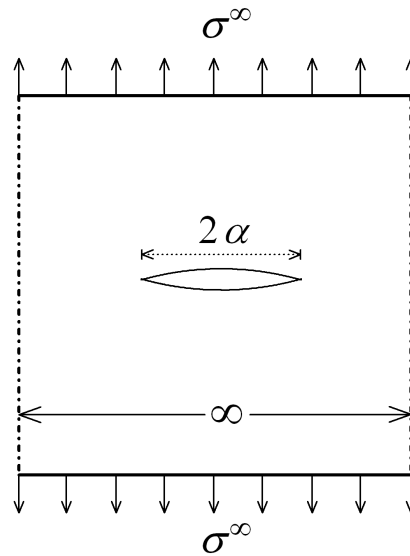
Figure 4.2: Center Cracked Panel.

following conditions are applied along the symmetry lines (Fig. 4.3b):

$$u_2 = 0, \quad \epsilon_{12} = 0, \quad \omega_3 = 0 \quad \text{on} \quad \text{AB}, \tag{4.6}$$

$$u_1 = 0, \quad \epsilon_{12} = 0, \quad \omega_3 = 0 \quad \text{on} \quad \text{DE}. \tag{4.7}$$
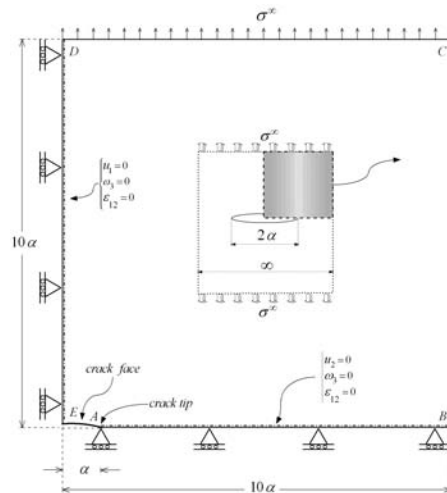
Figure 4.3: Center cracked panel.

The finite element mesh is shown in Fig. 4.4; all crack-tip nodes are tied together. The size of the smallest element in the focussed mesh at the crack-tip is $h = a/2000$, where a is the crack length as shown in Fig. 4.2.

Using dimensional analysis and taking into account that the solution is linear in σ^{∞}, we
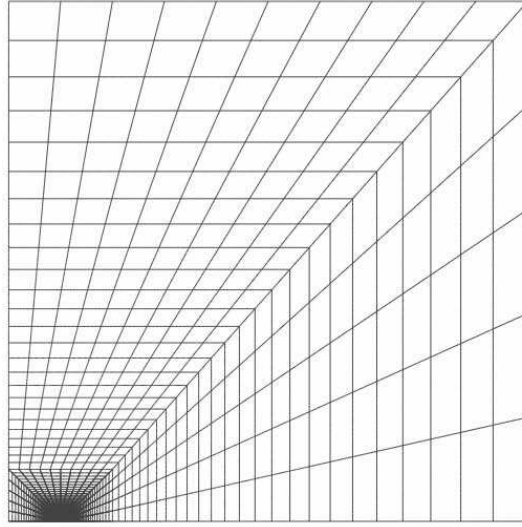
Figure 4.4: Finite element mesh.

conclude that one possible way to normalize the solution of the problem is as follows

$$\frac{\mathbf{u}}{a} = \frac{\sigma^\infty}{\mathrm{E}} \breve{\mathbf{u}}(\overbrace{\frac{r}{a}, \theta, \nu, \frac{\ell}{a}}^{q}) \quad \Rightarrow \quad \mathbf{u} = \frac{\sigma^\infty a}{\mathrm{E}} \breve{\mathbf{u}}(q), \tag{4.8}$$

$$\boldsymbol{\epsilon} = \frac{\sigma^\infty}{\mathrm{E}} \breve{\boldsymbol{\epsilon}}(q), \qquad \hat{\boldsymbol{\mu}} = \frac{\sigma^\infty}{a} \breve{\boldsymbol{\mu}}(q), \tag{4.9}$$

$$\frac{\boldsymbol{\tau}}{\mathrm{E}} = \frac{\sigma^\infty}{\mathrm{E}} \breve{\boldsymbol{\tau}}(\frac{r}{a}, \theta, \nu, \frac{\ell}{a}) \quad \Rightarrow \quad \boldsymbol{\tau} = \sigma^\infty \breve{\boldsymbol{\tau}}(q), \tag{4.10}$$

$$\frac{\boldsymbol{\sigma}}{\mathrm{E}} = \frac{\sigma^\infty}{\mathrm{E}} \breve{\boldsymbol{\sigma}}(\overbrace{\frac{r}{a}, \theta, \underbrace{\nu, \frac{\ell}{a}}_{\tilde{q}}}^{q}) \quad \Rightarrow \quad \boldsymbol{\sigma} = \sigma^\infty \breve{\boldsymbol{\sigma}}(q) \tag{4.11}$$

where q is the collection of dimensionless variables

$$q = \left\{ \frac{r}{a}, \theta, \nu, \frac{\ell}{a} \right\} \tag{4.12}$$

a is the crack length (see Fig. 4.2), and all functions with a superposed $\breve{}$ are dimensionless.

The asymptotic crack-tip solution for a mode-I crack is of the form (Aravas and Giannakopoulos [2])

$$u_1 = A\, x_1 + \ell \left(\frac{r}{\ell}\right)^{3/2} [A_1\, \tilde{u}_{11}(\theta, \nu) + A_2\, \tilde{u}_{12}(\theta, \nu)] + O(r^2), \tag{4.13}$$

$$u_2 = B\, x_2 + \ell \left(\frac{r}{\ell}\right)^{3/2} [A_1\, \tilde{u}_{21}(\theta, \nu) + A_2\, \tilde{u}_{22}(\theta, \nu)] + O(r^2),$$

where (x_1, x_2) and (r, θ) are crack-tip Cartesian and polar coordinates respectively, ν is Poisson's ratio, $\tilde{u}_{ij}$ are dimensionless functions, and (A, B, A_1, A_2) are constants determined by the complete solution of a boundary value problem. The A- and B-terms above correspond

to uniform normal strains parallel (ϵ_{11}) and normal (ϵ_{22}) to the crack line, which do not contribute to the crack-tip "energy release rate" (J-integral).

The dimensionless constants (A, B, A_1, A_2) in the asymptotic crack-tip solution are all proportional to $\frac{\sigma^\infty}{E}$. Therefore, we can write

$$A = \frac{\sigma^\infty}{E}\tilde{A}(\tilde{q}), \quad B = \frac{\sigma^\infty}{E}\tilde{B}(\tilde{q}), \quad A_1 = \frac{\sigma^\infty}{E}\tilde{A}_1(\tilde{q}), \quad A_2 = \frac{\sigma^\infty}{E}\tilde{A}_2(\tilde{q}), \tag{4.14}$$

where

$$\tilde{q} = \left\{\nu, \frac{\ell}{a}\right\} \tag{4.15}$$

so that

$$\tilde{A} = \lim_{r\to 0}\frac{\epsilon_{11}(r,\theta)}{\frac{\sigma^\infty}{E}}, \quad \tilde{B} = \lim_{r\to 0}\frac{\epsilon_{22}(r,\theta)}{\frac{\sigma^\infty}{E}}, \quad \tilde{A}_1 = \lim_{r\to 0}\frac{u_2(r,\pi)}{\frac{\sigma^\infty \ell}{E}\left(\frac{r}{\ell}\right)^{3/2}}, \quad \tilde{A}_2 = \lim_{r\to 0}\frac{-\omega_3(r,\pi)}{\frac{\sigma^\infty}{E}\sqrt{\frac{r}{\ell}}}. \tag{4.16}$$

The material data used in the calculations are $\nu = 0$ and $\ell = a/5$, so that the size of the crack-tip element relative to ℓ is $h = a/2000 = \ell/400$. The results of the finite element calculations are used for the evaluation of quantities that appear on the right hand side of equations (4.16). Considering the limits of these quantities as $r \to 0$, we conclude that for the particular geometry and material analyzed, i.e., for

$$\tilde{q} = (\nu, \frac{\ell}{a}) = (0, 0.2) \tag{4.17}$$

we have

$$\tilde{A} = 0.962, \qquad \tilde{B} = 2.292, \qquad \tilde{A}_1 = 3.165, \qquad \tilde{A}_2 = 3.433. \tag{4.18}$$

The results of the finite element solution are compared now to the predictions of the asymptotic solutions (Aravas and Giannakopoulos [2]) as $r \to 0$ under plane strain conditions ($u_3 = 0$). Let (r, θ) be crack-tip polar coordinates as shown in Fig. 4.5. The asymptotic solution on the crack face ($\theta = \pi$) is

$$u_1(r, \pi) = -A\,r + O(r^2), \tag{4.19}$$

$$u_2(r, \pi) = A_1\,\ell\left(\frac{r}{\ell}\right)^{3/2} + O(r^2), \tag{4.20}$$

$$\epsilon_{11}(r, \pi) = A + O(r), \tag{4.21}$$

$$\epsilon_{22}(r, \pi) = B + O(r), \tag{4.22}$$

$$\epsilon_{12}(r, \pi) = -\frac{3\,A_1 - 2\,A_2}{2}\sqrt{\frac{r}{\ell}} + O(r), \tag{4.23}$$

$$\omega_3(r, \pi) = -A_2\sqrt{\frac{r}{\ell}} + O(r). \tag{4.24}$$

Figures 4.6-4.8 show the radial variation of the finite element solution for (u_1, u_2, ω_3) on the crack face ($\theta = \pi$) together with the prediction of the asymptotic solution (equations (4.19),
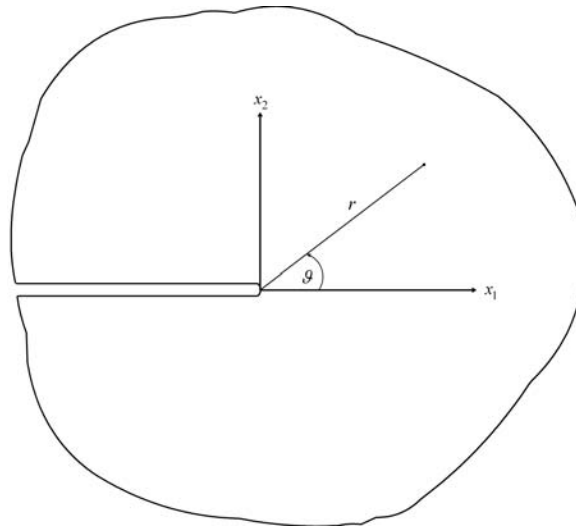
Figure 4.5: Crack-tip cartesian and polar coordinates.

(4.21), and (4.24)) on a logarithmic scale. The leading term in the asymptotic solution provides an accurate description of the displacement and rotation fields on $\theta = \pi$ in the range $0 < r < \ell/10$.
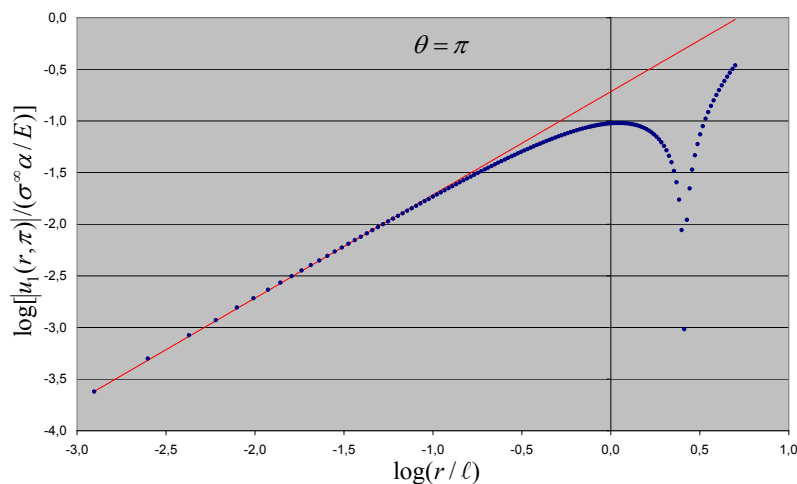
Figure 4.6: Variation of $\log \frac{u_1}{\sigma^\infty a/E}$ with $\log \frac{r}{\ell}$ along the crack face ($\theta = \pi$). The solid line represents the asymptotic crack-tip solution, and the dots the results of the finite element solution.
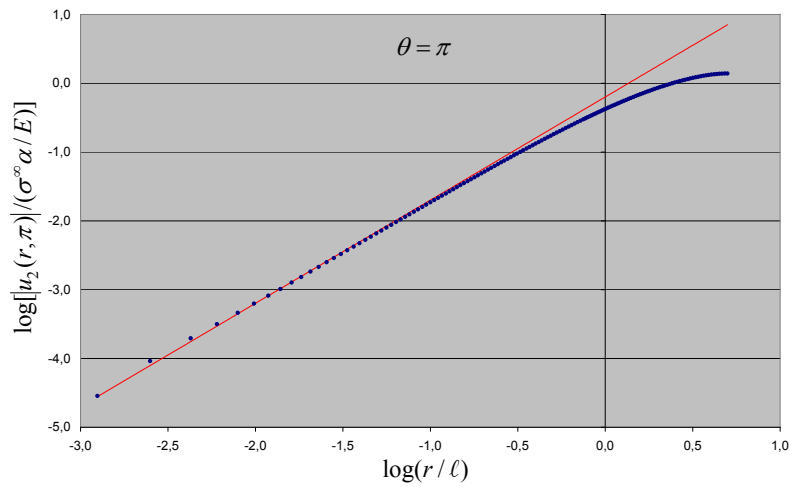
Figure 4.7: Variation of $\log \frac{u_2}{\sigma^\infty a/E}$ with $\log \frac{r}{\ell}$ along the crack face ($\theta = \pi$). The solid line represents the asymptotic crack-tip solution, and the dots the results of the finite element solution.
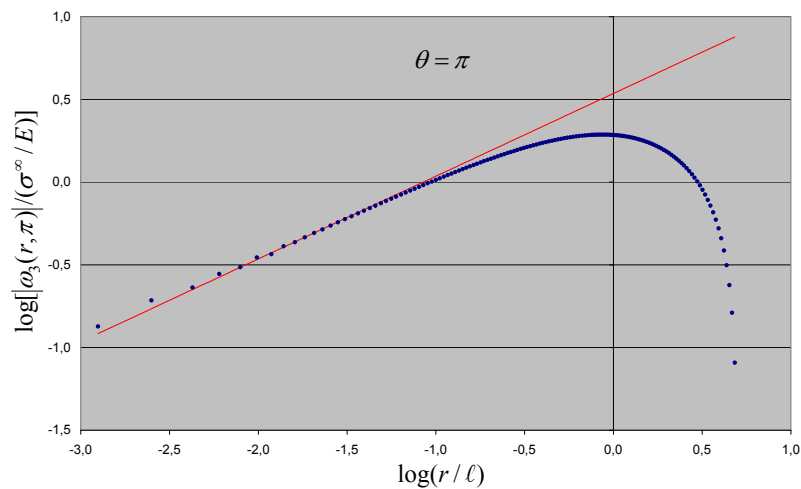
Figure 4.8: Variation of $\log \frac{|\omega_3|}{\sigma^\infty/E}$ with $\log \frac{r}{\ell}$ along the crack face ($\theta = \pi$). The solid line represents the asymptotic crack-tip solution, and the dots the results of the finite element solution.

Ahead of the crack ($\theta = 0$) the asymptotic solution is (Aravas and Giannakopoulos [2])

$$u_1(r,0) = A\,r + \frac{3\,A_1 - 2(3 - 4\,\nu)\,A_2}{12\,(1 - \nu)}\,\ell\,\left(\frac{r}{\ell}\right)^{3/2} + O(r^2), \qquad (4.25)$$

$$\epsilon_{11}(r,0) = A + \frac{3\,A_1 - 2\,(3 - 4\,\nu)\,A_2}{8\,(1 - \nu)}\sqrt{\frac{r}{\ell}} + O(r), \qquad (4.26)$$

$$\epsilon_{22}(r,0) = B - \frac{3\,A_1 + 2\,(1 - 4\,\nu)\,A_2}{8\,(1 - \nu)}\sqrt{\frac{r}{\ell}} + O(r), \qquad (4.27)$$

and $u_2(r,0) = 0$, $\epsilon_{12}(r,0) = \omega_3(r,0) = 0$.

Figure 4.9 shows the radial variation of the finite element solution for u_1 ahead of the crack ($\theta = 0$) together with the prediction of the asymptotic solution. Two curves are plotted for the asymptotic solution: curve I represents the leading term that involves A and B, whereas curve II is the sum of the first two terms on the right-hand side of (4.25).
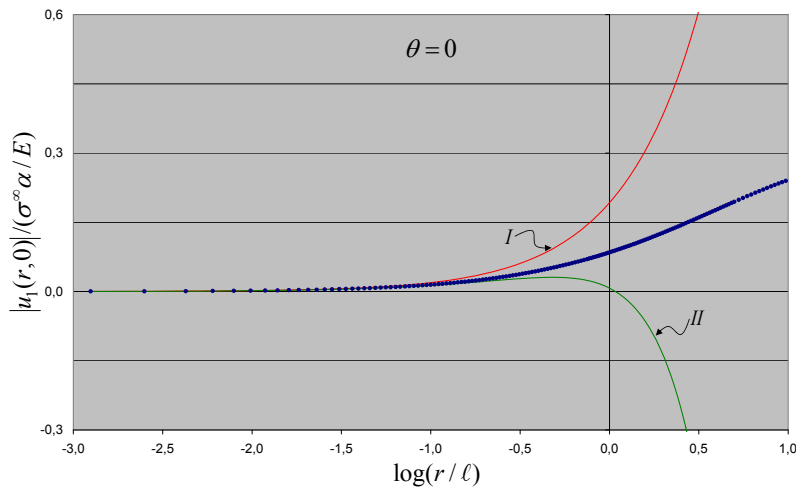
Figure 4.9: Variation of $\frac{u_1}{\sigma^\infty a/E}$ with $\log\frac{r}{\ell}$ ahead of the crack ($\theta = 0$). Curve I represents the leading term in the asymptotic expansion of the solution, curve II is the sum of the first two terms in the expansion, and the dots are the results of the finite element solution.

Figures 4.10 and 4.11 show the radial variation of the finite element solution for ϵ_{11} and ϵ_{22} on a logarithmic scale for $\theta = 0$ together with the prediction of the asymptotic solution; again, curves I represent the leading term that involve A and B, whereas curves II are the sum of the first two terms on the right-hand side of (4.26) and (4.27).
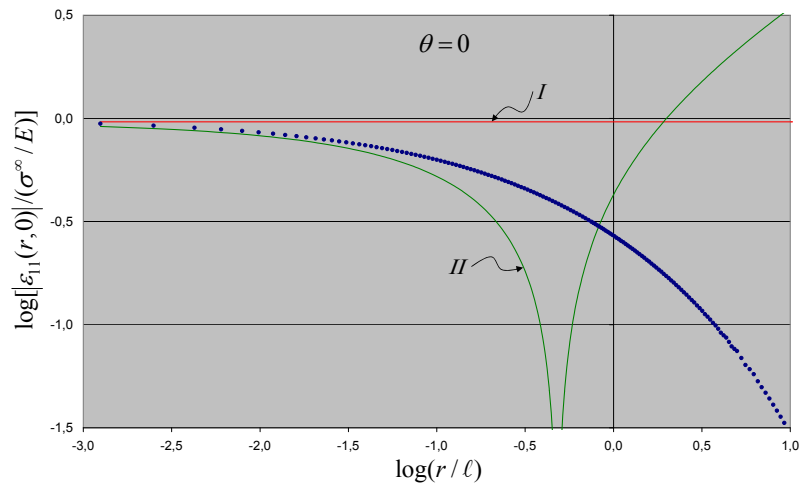
Figure 4.10: Variation of $\log \frac{|\epsilon_{11}|}{\sigma^\infty/E}$ ahead of the crack ($\theta = 0$). Curve I represents the leading term in the asymptotic expansion of the solution, curve II is the sum of the first two terms in the expansion, and the dots are the results of the finite element solution.
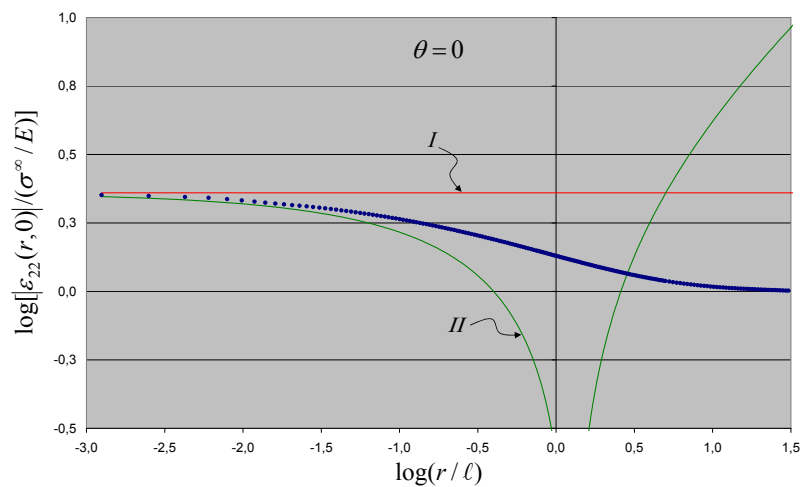
Figure 4.11: Variation of $\log \frac{|\epsilon_{22}|}{\sigma^\infty/E}$ ahead of the crack ($\theta = 0$). Curve I represents the leading term in the asymptotic expansion of the solution, curve II is the sum of the first two terms in the expansion, and the dots are the results of the finite element solution.

As Aravas and Giannakopoulos [2] pointed out, the constants A and B provide the limiting values of ϵ_{11} and ϵ_{22} as $r \to 0$, but the second term in the asymptotic expansion is required for an accurate description of the strain state ahead of the crack for radial distances of order $\ell/10$.

Figures 4.12-4.17 show the angular variation of the normalized components of $\mathbf{u}$, $\boldsymbol{\epsilon}$ and ω_3 at various radial distances form the crack-tip together with the corresponding prediction of the leading term in the asymptotic crack-tip solution. In particular, the angular variation of the following quantities is plotted:

$$\left\{ \frac{u_1/r}{\sigma^\infty/E}, \ \frac{u_2/r}{\sigma^\infty/E}, \ \frac{\epsilon_{11}}{\sigma^\infty/E}, \ \frac{\epsilon_{22}}{\sigma^\infty/E}, \ \frac{2\epsilon_{12}/\sqrt{r/\ell}}{\sigma^\infty/E}, \ \frac{\omega_3/\sqrt{r/\ell}}{\sigma^\infty/E} \right\}. \tag{4.28}$$

In view of the normalization used, all curves for each of the aforementioned normalized quantities should fall on a single curve for values of r inside the "region of dominance" of the leading term in the asymptotic crack-tip solution. Figures 4.12-4.17 show that the leading term in the asymptotic solution provides an accurate description of the crack-tip fields over radial distances of order $\ell/10$.
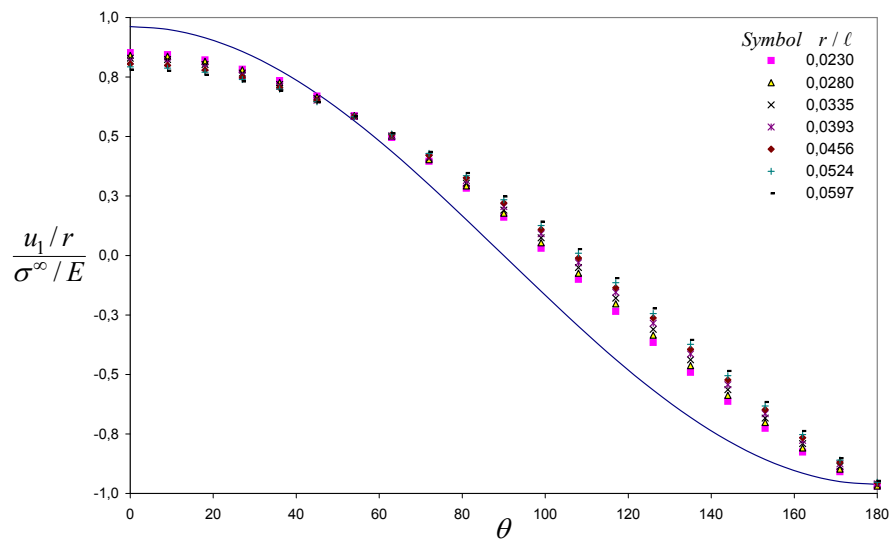
Figure 4.12: Angular variation of $\frac{u_1/r}{\sigma^\infty/E}$ at various radial distances. The solid line represents the asymptotic crack-tip solution.
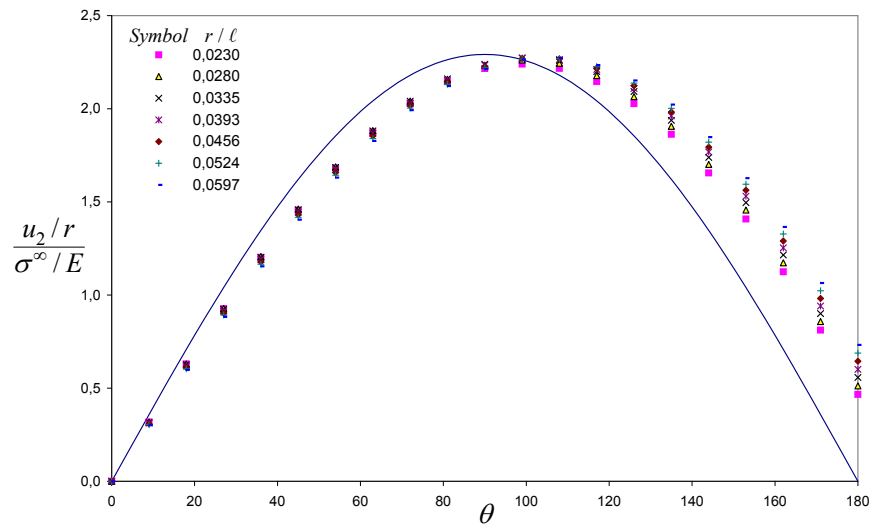
Figure 4.13: Angular variation of $\frac{u_2/r}{\sigma^\infty/E}$ at various radial distances. The solid line represents the asymptotic crack-tip solution.
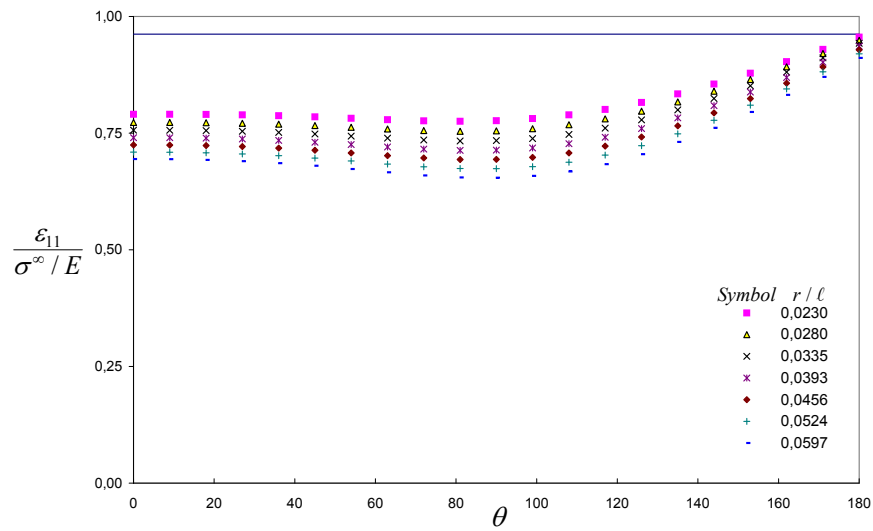
Figure 4.14: Angular variation of $\frac{\epsilon_{11}}{\sigma^\infty/E}$ at various radial distances. The solid line represents the asymptotic crack-tip solution.
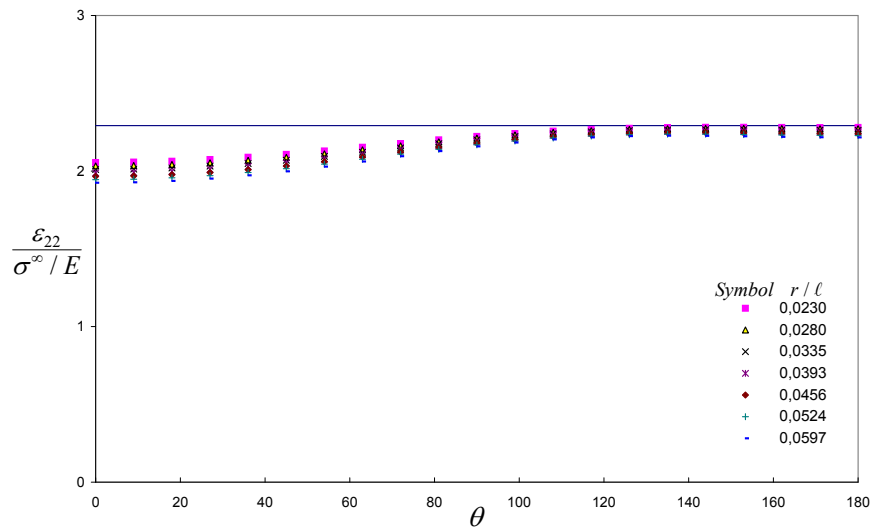
Figure 4.15: Angular variation of $\frac{\epsilon_{22}}{\sigma^\infty/E}$ at various radial distances. The solid line represents the asymptotic crack-tip solution.
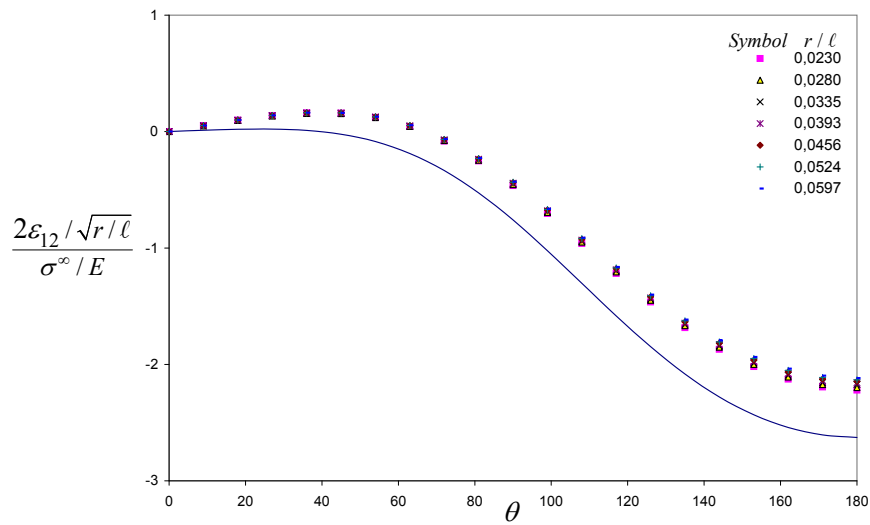
Figure 4.16: Angular variation of $\frac{2\epsilon_{12}/\sqrt{r/\ell}}{\sigma^\infty/E}$ at various radial distances. The solid line represents the asymptotic crack-tip solution.
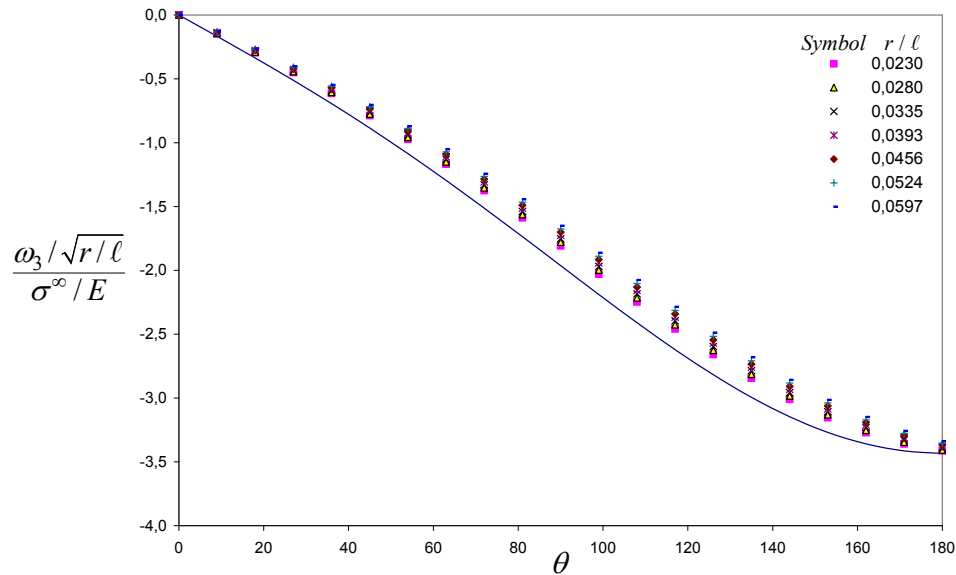
Figure 4.17: Angular variation of $\frac{\omega_3/\sqrt{r/\ell}}{\sigma^\infty/E}$ at various radial distances. The solid line represents the asymptotic crack-tip solution.

In the finite element formulation of Amanatidou and Aravas [1] the true stress in a finite element solution is calculated by using the equations

$$\sigma_{ij} = \bar{\sigma}_{ij} + \bar{\sigma}_{ij}^{(2)} = \frac{\partial \bar{W}}{\partial u_{(i,j)}} + \bar{\sigma}_{ij}^{(2)}. \tag{4.29}$$

The results of the finite element solution are compared now to the predictions of the crack-tip asymptotic solution (Aravas and Giannakopoulos [2]).

For comparison purposes, we carried out finite element calculations for the same specimen geometry and applied loads using the corresponding classical isotropic linear elasticity model ($\nu = 0$, $\ell = 0$). Eight-node plane strain isoparametric elements with 3×3 Gauss integration stations are used in the calculations. Again, all crack-tip nodes are tied together.

Figure 4.18 shows the variation of the normalized true stress $\sigma_{22}/\sigma^\infty$ as a function of the normalized radial distance r/ℓ along the radial line $\theta = \frac{\pi}{40}$ for both the gradient and classical elasticity solutions.
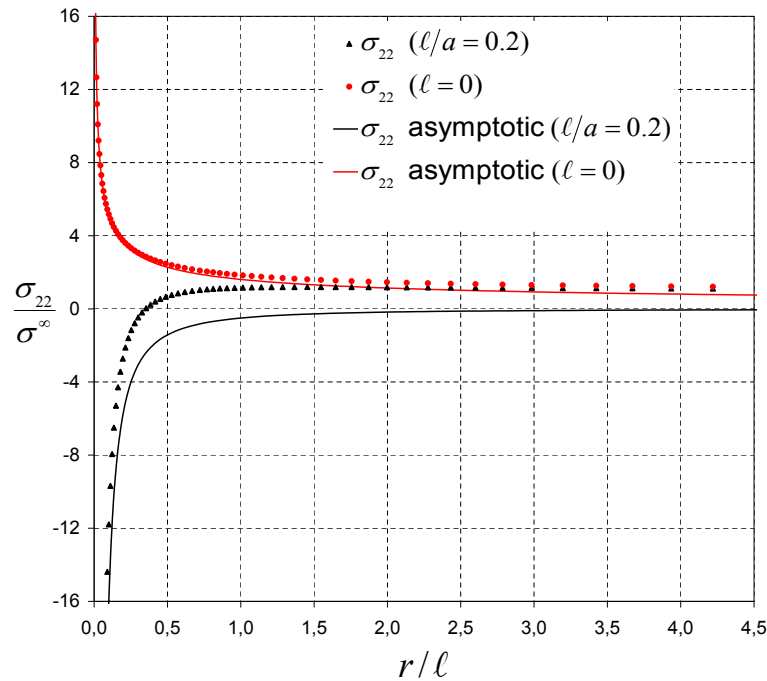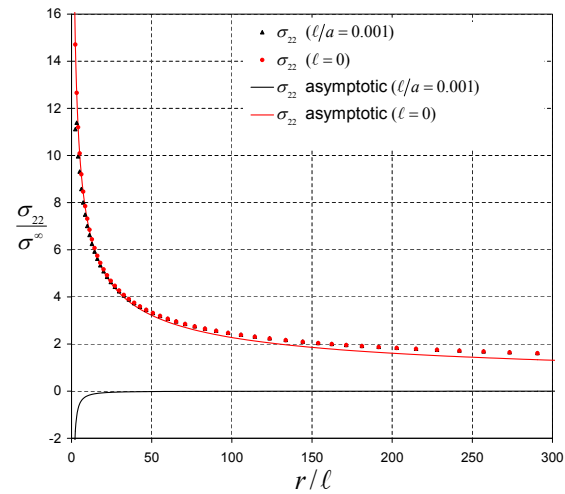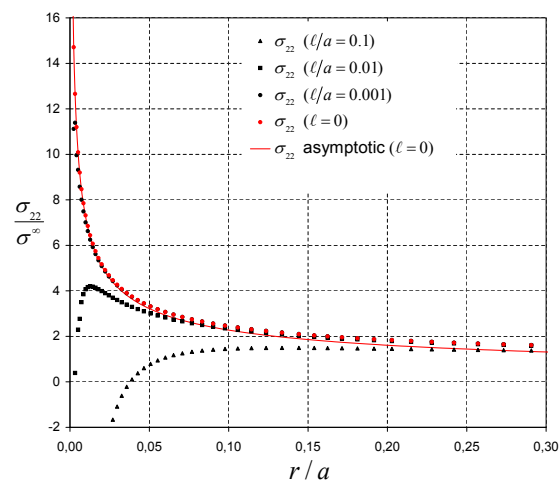
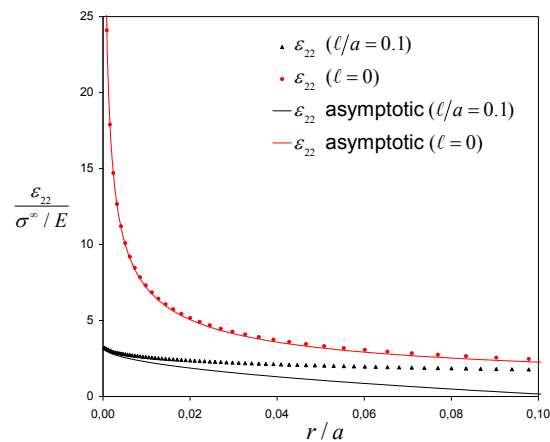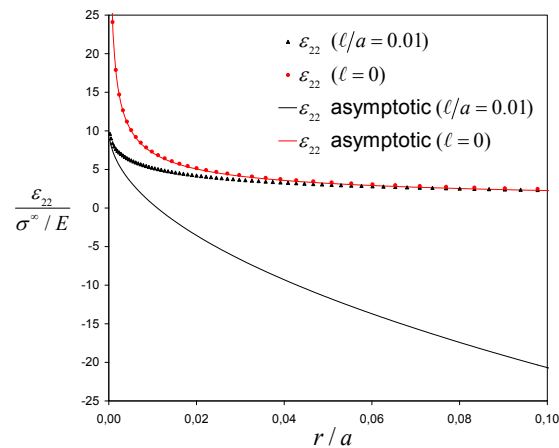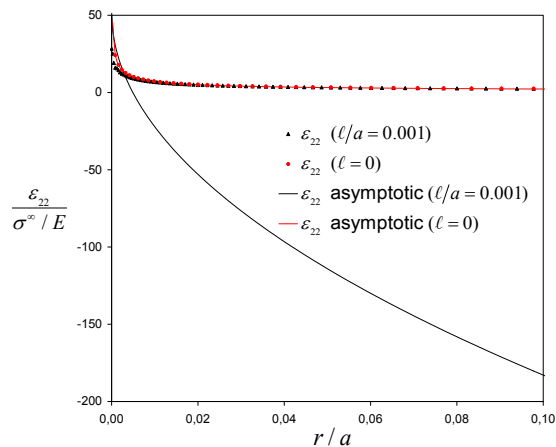Figure 4.18: Variation of the normalized true stress $\sigma_{22}/\sigma^\infty$ as a function of the normalized radial distance r/ℓ ahead of the crack. The classical solution is also shown for comparison.

In gradient elasticity, this full-field result shows the existence of a maximum tensile value of σ_{22}, at a distance $r/\ell \simeq 1$ ahead of the crack, in accord to what has been reported by various researchers and recently by Aravas and Giannakopoulos [2] for the ECP geometry. This maximum value increases monotonically to infinity as $\ell \to 0$. We observe also that the region of validity of the asymptotic solution in gradient elasticity is comparable to that of the classical solution ($\ell = 0$).

For the specimen geometry and applied loads considered above, we carry out finite element calculations with $\ell/a = 0., 0.001, 0.01, 0.1$. Again the value $\nu = 0$ is used for Poisson's ratio. For each value of ℓ, two sets of calculations are carried out: one with normalized true stress σ_{22} and another with normalized normal strain ϵ_{22} as a function of the normalized radial distance r, for the gradient and classical elasticity solutions. In the gradient elasticity solution σ_{22} reaches a maximum at $r \simeq \ell$.

Figures 4.19-4.22 show the variation of the normalized true stress $\sigma_{22}/\sigma^\infty$ as a function of the normalized radial distance r/ℓ along the radial line $\theta = \frac{\pi}{40}$ for both the gradient and classical elasticity solutions.
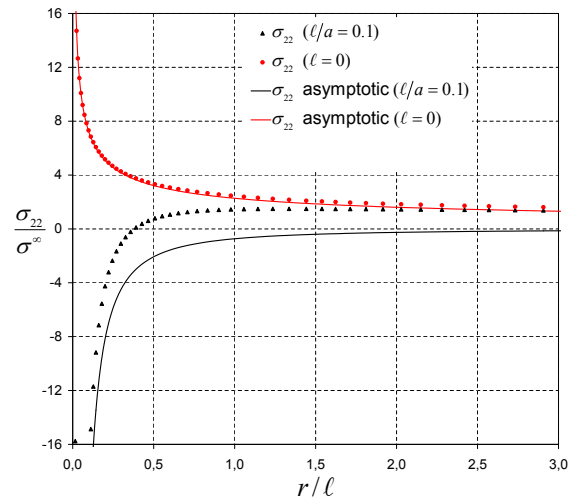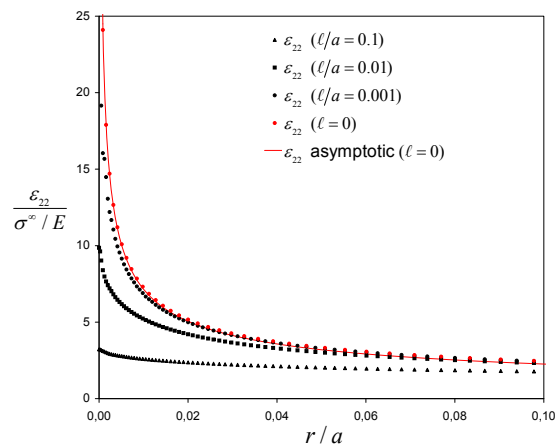
Figure 4.19: Variation of the normalized true stress $\sigma_{22}/\sigma^{\infty}$ as a function of the normalized radial distance r/ℓ along the radial line $\theta = \frac{\pi}{40}$ for both the gradient and classical elasticity solutions.
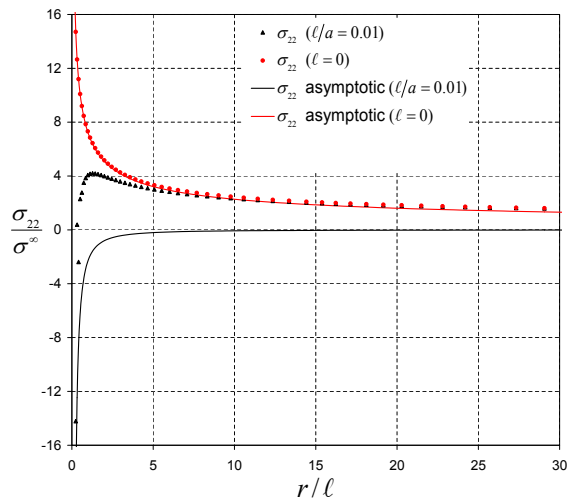
Figure 4.20: Variation of the normalized true stress $\sigma_{22}/\sigma^{\infty}$ as a function of the normalized radial distance r/ℓ along the radial line $\theta = \frac{\pi}{40}$ for both the gradient and classical elasticity solutions.

Figure 4.21: Variation of the normalized true stress $\sigma_{22}/\sigma^\infty$ as a function of the normalized radial distance r/ℓ along the radial line $\theta = \frac{\pi}{40}$ for both the gradient and classical elasticity solutions.

Figure 4.22: Variation of the normalized true stress $\sigma_{22}/\sigma^\infty$ as a function of the normalized radial distance r/α along the radial line $\theta = \frac{\pi}{40}$ for both the gradient and classical elasticity solutions.

Figures 4.23-4.26 show the variation of the normalized normal strain ϵ_{22} ahead of the crack ($\theta = 0$) for the gradient and classical elasticity solutions.

Figure 4.23: Variation of the normalized normal strain $\epsilon_{22}/(\sigma^\infty/E)$ as a function of the normalized radial distance r/a along the radial line $\theta = 0$ for both the gradient and classical elasticity solutions.

Figure 4.24: Variation of the normalized normal strain $\epsilon_{22}/(\sigma^\infty/E)$ as a function of the normalized radial distance r/a along the radial line $\theta = 0$ for both the gradient and classical elasticity solutions.

Figure 4.25: Variation of the normalized normal strain $\epsilon_{22}/(\sigma^\infty/E)$ as a function of the normalized radial distance r/a along the radial line $\theta = 0$ for both the gradient and classical elasticity solutions.

Figure 4.26: Variation of the normalized normal strain $\epsilon_{22}/(\sigma^\infty/E)$ as a function of the normalized radial distance r/a along the radial line $\theta = 0$ for both the gradient and classical elasticity solutions.

Figures 4.27-4.34 show the normalized components of σ_{11}, σ_{22}, $\sigma_{(12)}$ and $\sigma_{[12]}$ as a function of the normalized radial distance r/ℓ along the radial lines $\theta = \frac{\pi}{40}$ and $\theta = \pi - \frac{\pi}{40}$ together with the corresponding prediction of the asymptotic crack-tip solution on a logarithmic scale.
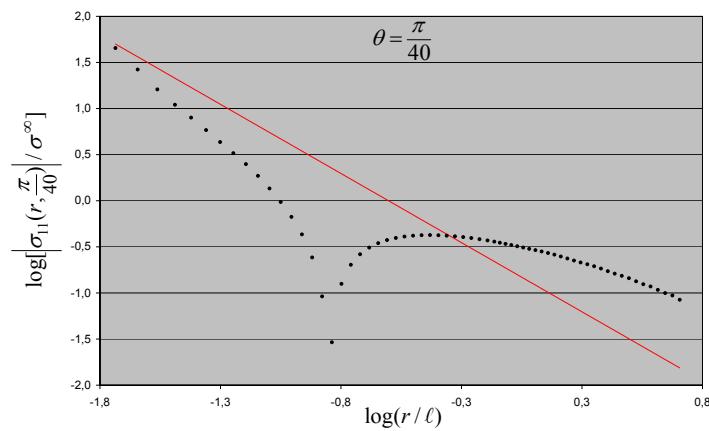
Figure 4.27: Variation of $\log[|\sigma_{11}(r, \frac{\pi}{40})|/\sigma^{\infty}]$ with $\log \frac{r}{\ell}$ along the radial line $\theta = \frac{\pi}{40}$. The solid line represents the asymptotic crack-tip solution, and the dots the results of the finite element solution.
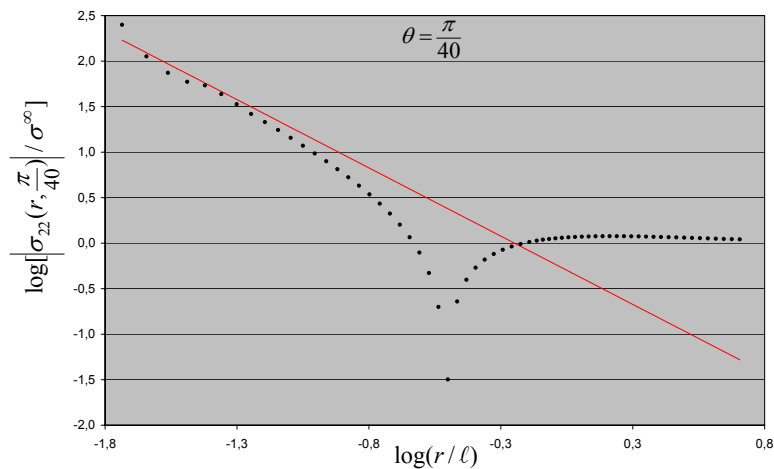
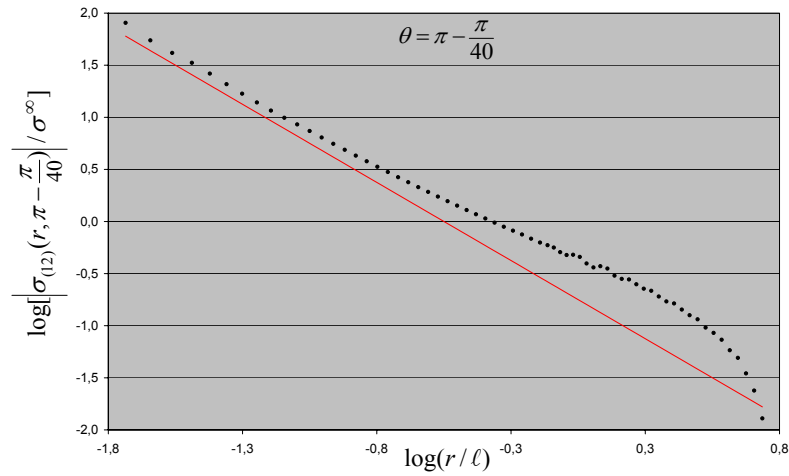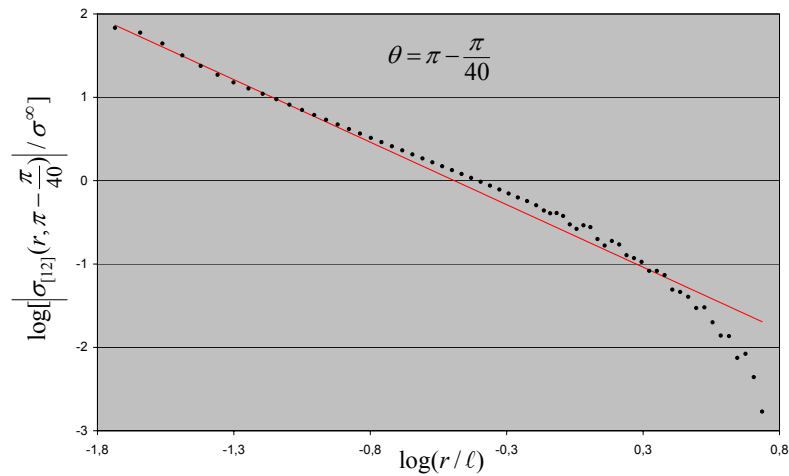Figure 4.28: Variation of $\log[|\sigma_{22}(r, \frac{\pi}{40})|/\sigma^{\infty}]$ with $\log \frac{r}{\ell}$ along the radial line $\theta = \frac{\pi}{40}$. The solid line represents the asymptotic crack-tip solution, and the dots the results of the finite element solution.
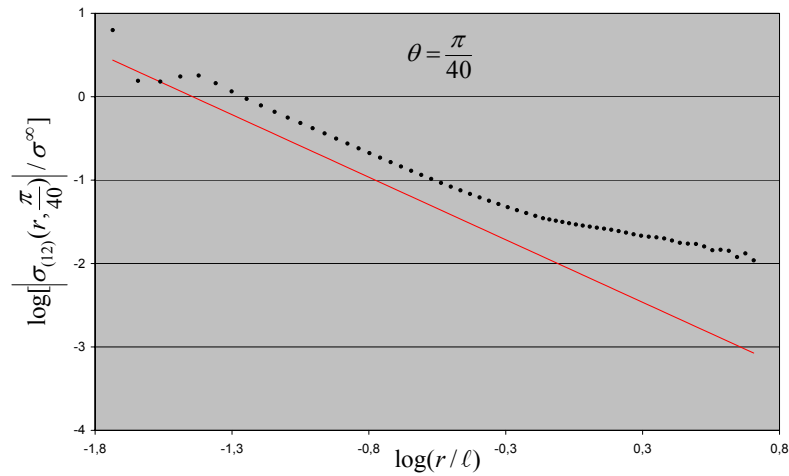
Figure 4.29: Variation of $\log[\left|\sigma_{(12)}(r, \frac{\pi}{40})\right|/\sigma^{\infty}]$ with $\log\frac{r}{\ell}$ along the radial line $\theta = \frac{\pi}{40}$. The solid line represents the asymptotic crack-tip solution, and the dots the results of the finite element solution.
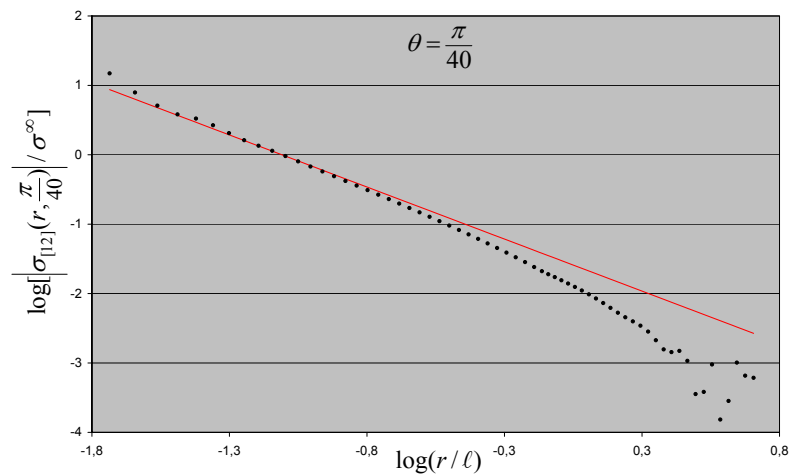
Figure 4.30: Variation of $\log[\left|\sigma_{[12]}(r, \frac{\pi}{40})\right|/\sigma^{\infty}]$ with $\log\frac{r}{\ell}$ along the radial line $\theta = \frac{\pi}{40}$. The solid line represents the asymptotic crack-tip solution, and the dots the results of the finite element solution.
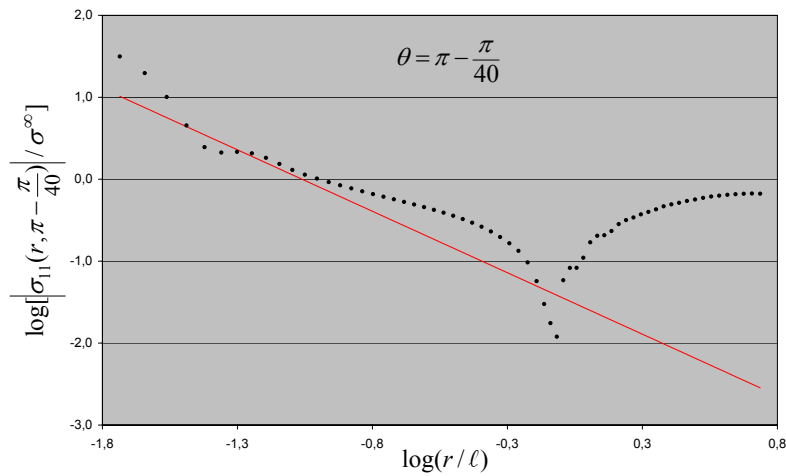
Figure 4.31: Variation of $\log\left[\left|\sigma_{11}(r, \pi - \frac{\pi}{40})\right|/\sigma^{\infty}\right]$ with $\log\frac{r}{\ell}$ along the radial line $\theta = \pi - \frac{\pi}{40}$. The solid line represents the asymptotic crack-tip solution, and the dots the results of the finite element solution.
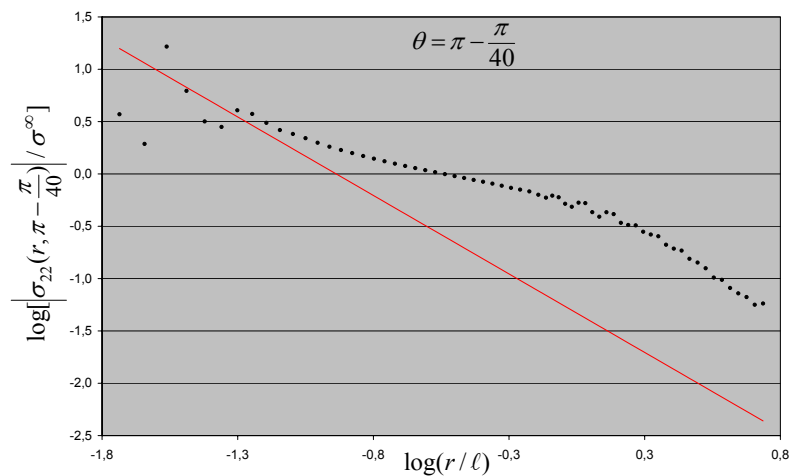
Figure 4.32: Variation of $\log\left[\left|\sigma_{22}(r, \pi - \frac{\pi}{40})\right|/\sigma^{\infty}\right]$ with $\log\frac{r}{\ell}$ along the radial line $\theta = \pi - \frac{\pi}{40}$. The solid line represents the asymptotic crack-tip solution, and the dots the results of the finite element solution.

Figure 4.33: Variation of $\log\left[\left|\sigma_{(12)}(r, \pi - \frac{\pi}{40})\right|/\sigma^\infty\right]$ with $\log\frac{r}{\ell}$ along the radial line $\theta = \pi - \frac{\pi}{40}$. The solid line represents the asymptotic crack-tip solution, and the dots the results of the finite element solution.

Figure 4.34: Variation of $\log\left[\left|\sigma_{[12]}(r, \pi - \frac{\pi}{40})\right|/\sigma^\infty\right]$ with $\log\frac{r}{\ell}$ along the radial line $\theta = \pi - \frac{\pi}{40}$. The solid line represents the asymptotic crack-tip solution, and the dots the results of the finite element solution.

Figures 4.35-4.38 show the angular variation of the normalized components of σ_{11}, σ_{22}, $\sigma_{(12)}$ and $\sigma_{[12]}$ at various radial distances from the crack-tip together with the corresponding prediction of the asymptotic crack-tip solution. In particular, the angular variation of the following quantities is plotted:

$$\left\{ \frac{\sigma_{11}/\sigma^\infty}{(r/\ell)^{\frac{3}{2}}}, \; \frac{\sigma_{22}/\sigma^\infty}{(r/\ell)^{\frac{3}{2}}}, \; \frac{\sigma_{(12)}/\sigma^\infty}{(r/\ell)^{\frac{3}{2}}}, \; \frac{\sigma_{[12]}/\sigma^\infty}{(r/\ell)^{\frac{3}{2}}} \right\}. \tag{4.30}$$
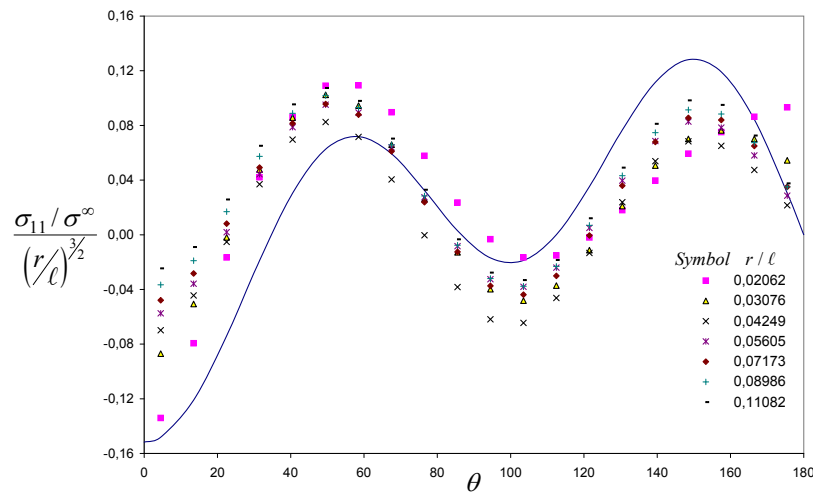
Figure 4.35: Angular variation of the normalized true stress $\frac{\sigma_{11}/\sigma^\infty}{(r/\ell)^{3/2}}$ at various radial distances. The solid line represents the asymptotic crack-tip solution.
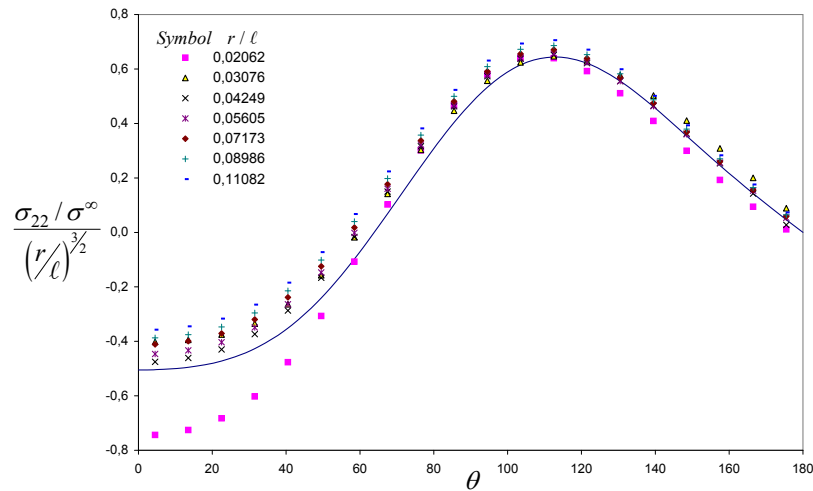
Figure 4.36: Angular variation of the normalized true stress $\frac{\sigma_{22}/\sigma^\infty}{\left(\frac{r}{\ell}\right)^{\frac{3}{2}}}$ at various radial distances. The solid line represents the asymptotic crack-tip solution.
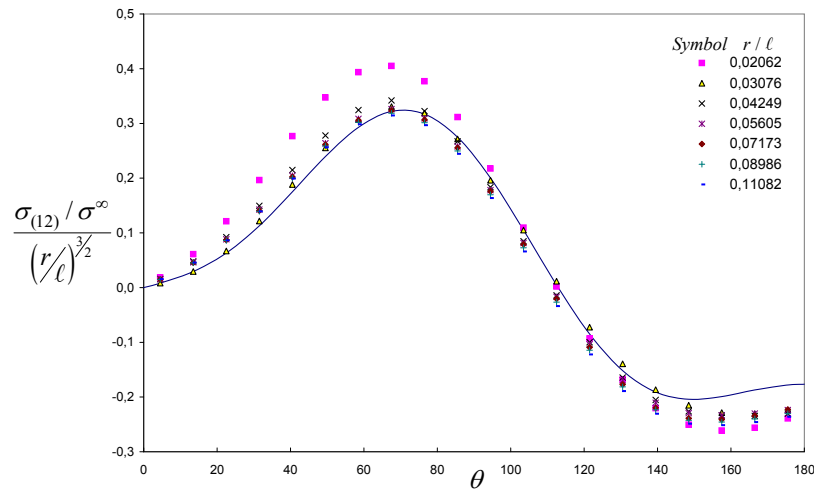
Figure 4.37: Angular variation of the normalized true stress $\frac{\sigma_{(12)}/\sigma^\infty}{\left(\frac{r}{\ell}\right)^{\frac{3}{2}}}$ at various radial distances. The solid line represents the asymptotic crack-tip solution.
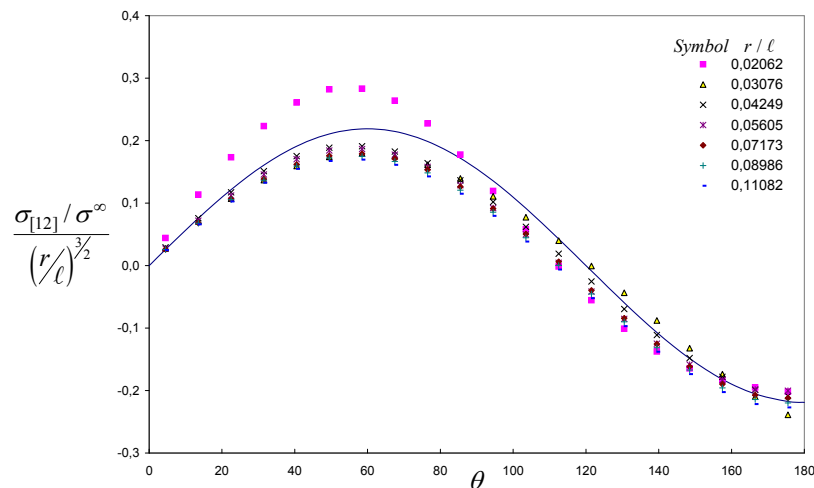
Figure 4.38: Variation of the normalized true stress $\frac{\sigma_{[12]}/\sigma^\infty}{\left(\frac{r}{\ell}\right)^{\frac{3}{2}}}$ at various radial distances. The solid line represents the asymptotic crack-tip solution.

Figure 4.39a shows the profile of the crack face for $\ell = 0$ and $\ell/a = 0.2$, together with the predictions of the corresponding asymptotic solutions. The cusp-like crack opening characterizes the gradient elasticity solution and has been observed also by Karlis *et al.* [12, 13] and by Aravas and Giannakopoulos [2] in their studies of the central crack and edge crack geometry respectively. Figure 4.39b shows the profiles of the crack face for the gradient case and for different values of ℓ/a.
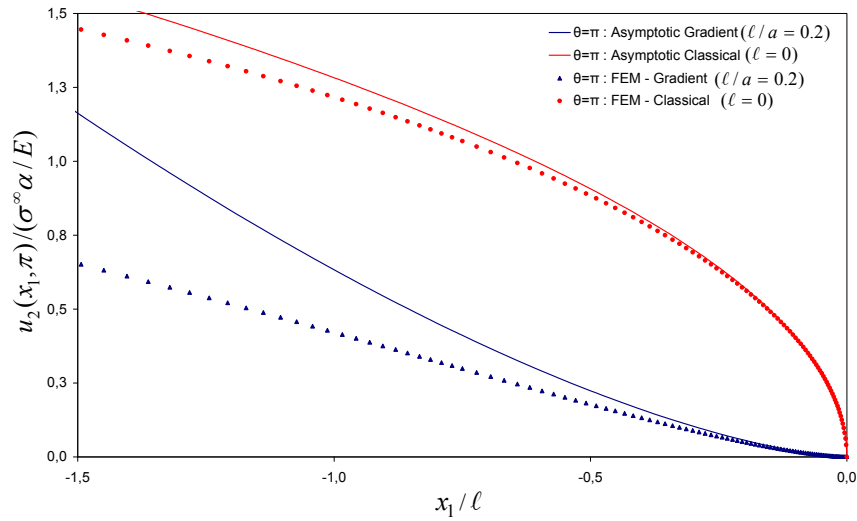
(a)
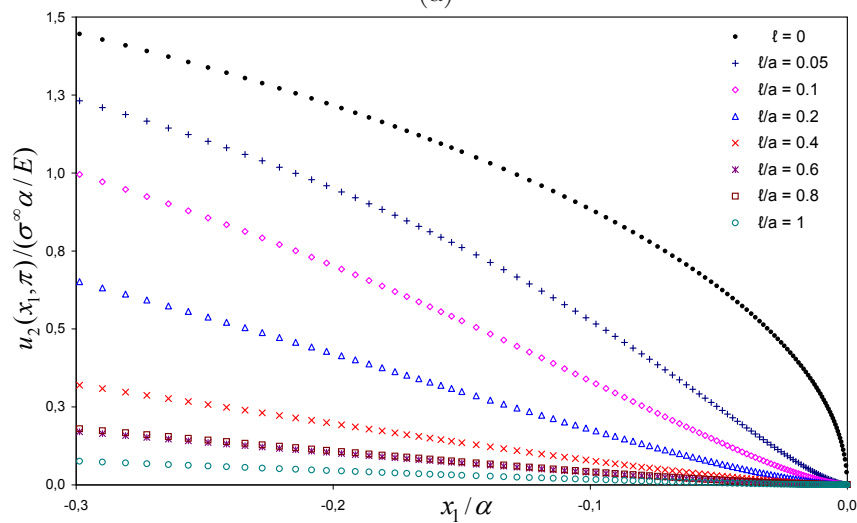
(b)

Figure 4.39: Crack profiles $u_2(x_1, \pi)/(\sigma^\infty \alpha / E)$ for gradient elasticity: (a) asymptotic and finite element solutions for $\ell = 0$ and $\ell/a = 0.2$, (b) finite element results for different values of ℓ.

Gavardinas [5] conducted qualitative experiments concerning the prediction for the mechanical behavior (e.g. the shape for the crack opening) of textile materials with microstructure. Typical fracture mechanics cracked configurations were examined. The specimens were confined into transparent plexiglass to enforce plane strain conditions.

Figure 4.40 shows the left crack-tip of a polymer-impregnated textile with a double-edge crack loaded in tension. The crack length a is 1 cm and the internal length ℓ (woven matrix) is 0.1 cm ($\ell/a = 0.1$). No bridging effect and complete closure are observed upon unloading. The figure shows clearly the formation of a cusp at the crack-tip and indicates the possibility of using gradient elasticity theory in order to describe the mechanical behavior of textile composites.

(a)

(b)

Figure 4.40: Formation of a cusp at the crack-tip of a polymer-impregnated textile with a double-edge crack loaded in tension ($\ell/a = 0.1$).

Figure 4.41 shows contours of the normal strain ϵ_{22} in the crack tip region for the two theories (classical and gradient). The major difference in the two solutions is that the finite (asymptotically constant) strains of the gradient elasticity solution at the crack-tip are replaced by singular $(1/\sqrt{r})$ strains in the classical solution $(\ell = 0)$.
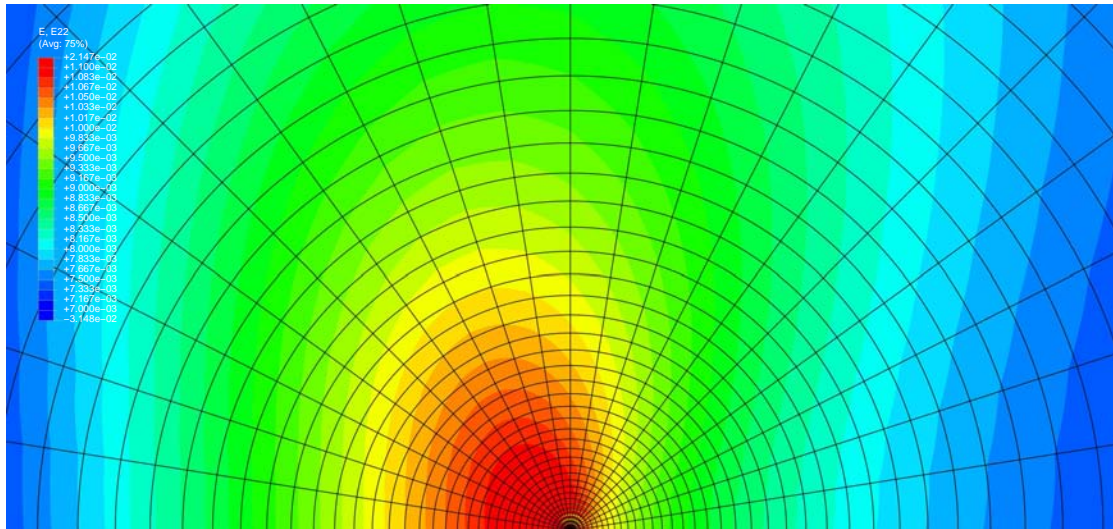
(a)
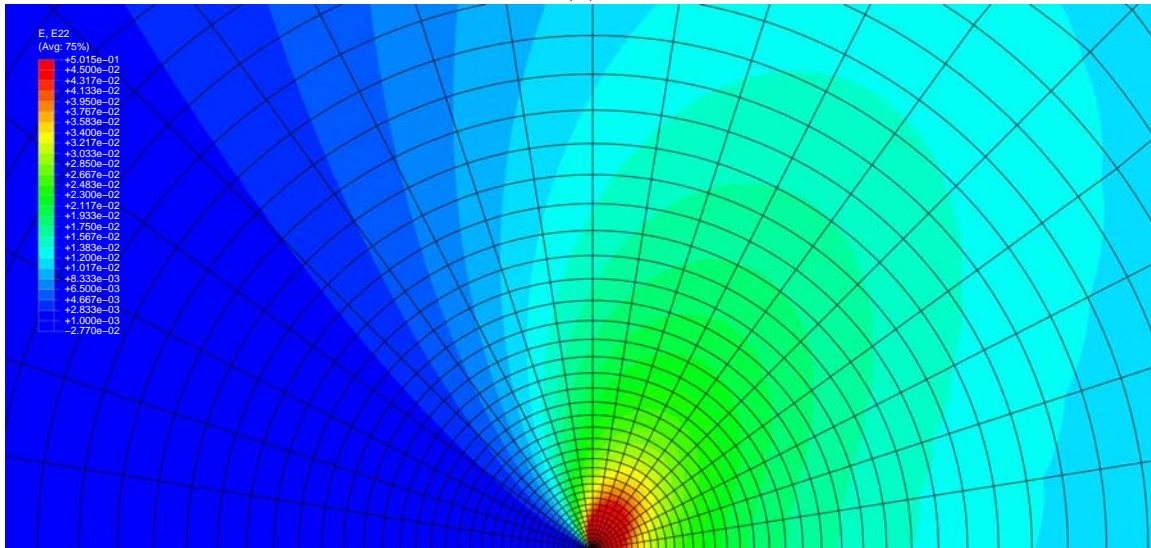
(b)

Figure 4.41: Contour plots of the normal strain ϵ_{22} in the crack-tip region: (a) gradient elasticity $(\ell/a = 0.2)$, (b) classical elasticity $(\ell = 0)$.
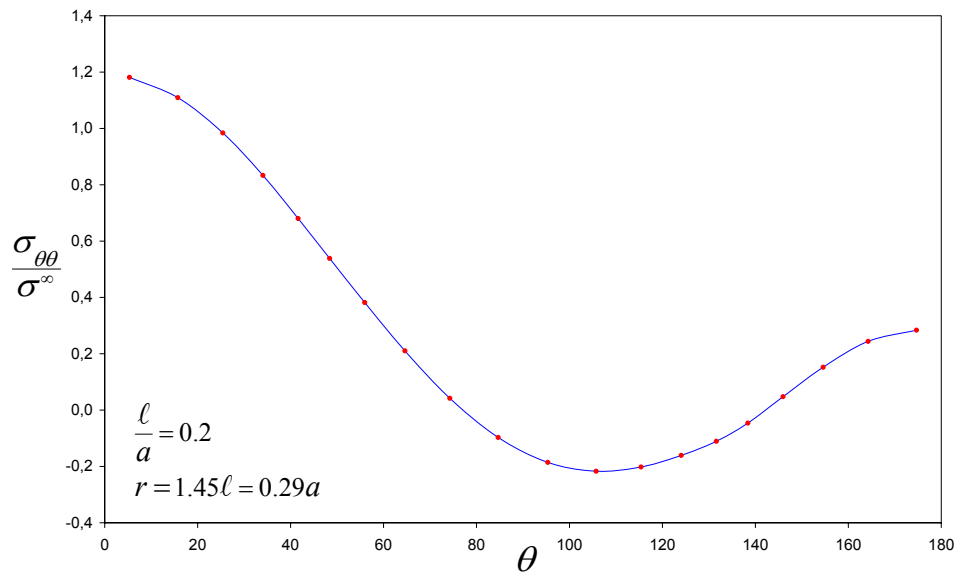
Figure 4.42: Angular variation of the normalized $\sigma_{\theta\theta}/\sigma^{\infty}$ at the radial distance at which $\sigma_{\theta\theta}$ maximizes ahead of the crack.

Figure 4.42 shows the angular variation of the normalized component of $\sigma_{\theta\theta}$ at the radial distance where $\sigma_{\theta\theta}$ reaches a maximum ahead of the crack. At that radial distance, the maximum value of $\sigma_{\theta\theta}$ appears at $\theta = 0$. It emphasized though that this is not the case for an edge-cracked panel (ECP). As discussed in the following section, the corresponding maximum value of $\sigma_{\theta\theta}$ for the ECP appears at $\theta \simeq 100°$.

The results of the finite element calculations are used for the evaluation of the quantities that appear on the right hand side of equations 4.16 and the radial distance $r_{\max}$ at which $\sigma_{\theta\theta}$ maximizes ahead ($\theta = 0$) of the crack (Fig. 4.43) where ℓ is the internal length and a is the crack length of the problem under consideration..

Center Cracked Panel

ℓ/a	$\tilde{A}_1$	$\tilde{A}_2$	$\tilde{A}$	$\tilde{B}$	$r_{\max}/\ell$
0.001	37.388	37.945	19.879	52.16	3.22
0.01	14.786	17.026	6.901	10.308	1.27
0.1	4.700	5.299	1.779	3.251	1.34
0.2	3.165	3.433	0.962	2.292	1.45

Figure 4.43: Variation of the quantities that appear on the right hand side of equations (4.16 with the normalized radial distance $r_{\max}$ at which $\sigma_{\theta\theta}$ maximizes ahead ($\theta = 0$) of the crack.

Chapter 5

Finite Element Solutions - Edge Cracked Panel (ECP)

In this chapter, for comparison purposes, we carry out finite element calculations of another cracked specimen. We consider the plane strain problem of an edge-cracked panel (ECP) loaded with two concentrated forces as shown in Fig. 5.1. Both the specimen and the applied loads are symmetric with respect to the crack plane (mode-I).
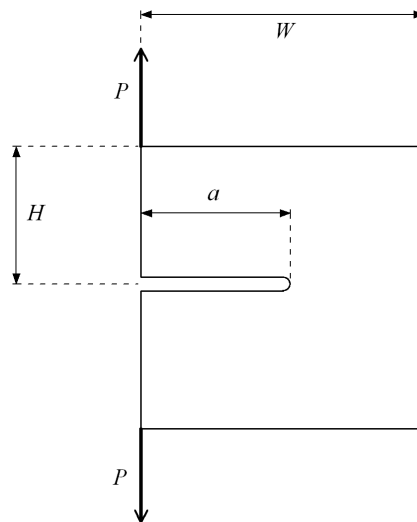

Figure 5.1: Edge Cracked Panel.

The problem is solved again by using the finite element formulation of Amanatidou and Aravas [1], which was implemented in the ABAQUS general purpose finite element program. Nine-node elements (III9-70 in [1]) are used in the computations. Because of symmetry, only half of the specimen is analyzed and the following conditions are applied along the symmetry line ahead of the crack:

$$u_2 = 0, \qquad \epsilon_{12} = 0, \qquad \omega_3 = 0. \tag{5.1}$$

In the following, we discuss in detail the variation of the true stress components. Figures 5.2-5.9 show the normalized components of σ_{11}, σ_{22}, $\sigma_{(12)}$ and $\sigma_{[12]}$ as a function of the

normalized radial distance r/ℓ along the radial lines $\theta = \frac{\pi}{40}$ and $\theta = \pi - \frac{\pi}{40}$ together with the corresponding prediction of the asymptotic crack-tip solution on a logarithmic scale.
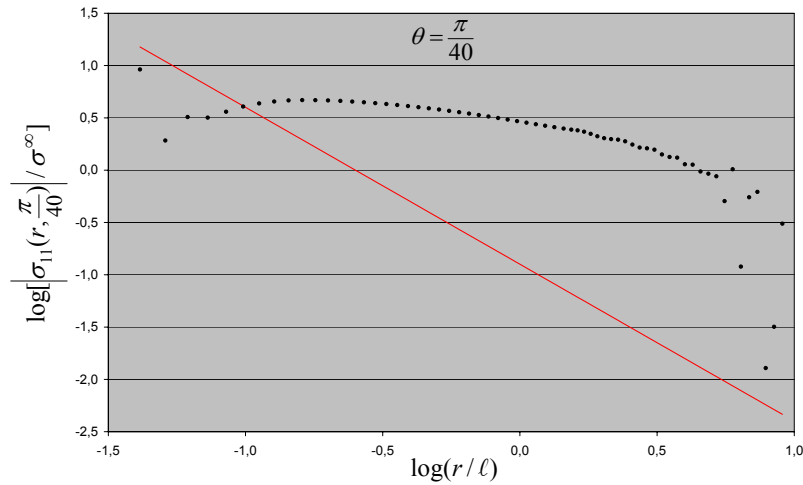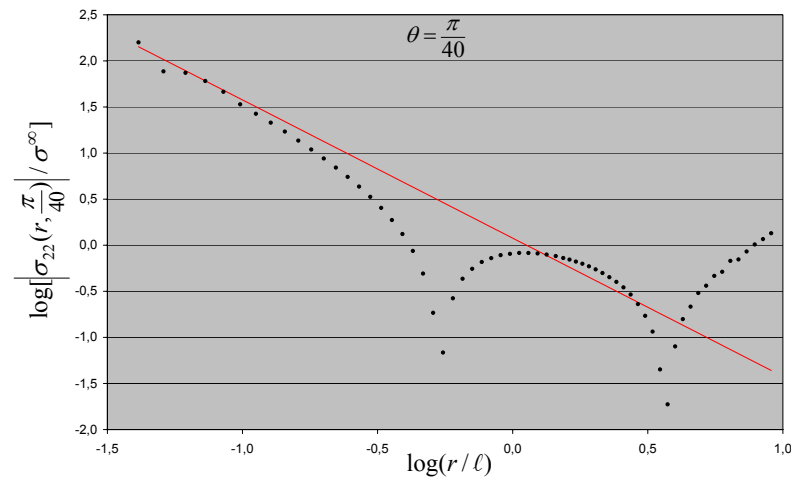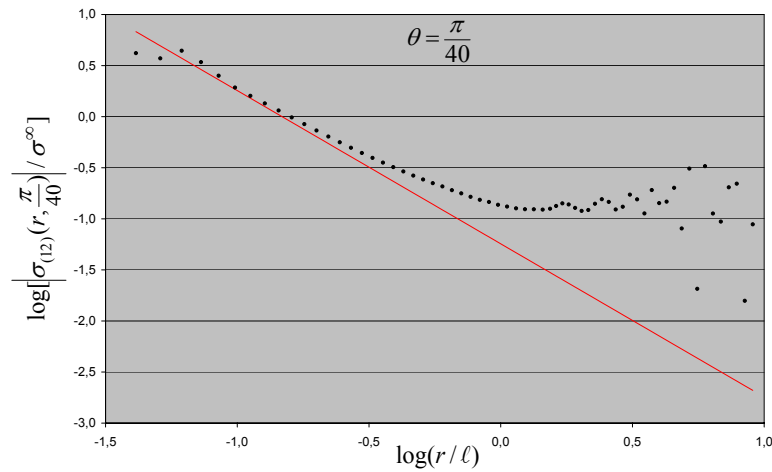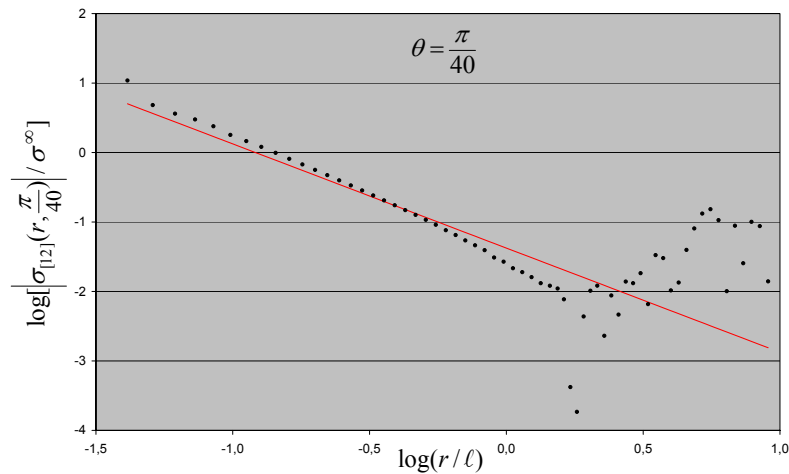

Figure 5.2: Variation of $\log[\left|\sigma_{11}(r, \frac{\pi}{40})\right|/\sigma^{\infty}]$ with $\log \frac{r}{\ell}$ along the radial line $\theta = \frac{\pi}{40}$. The solid line represents the asymptotic crack-tip solution, and the dots the results of the finite element solution.
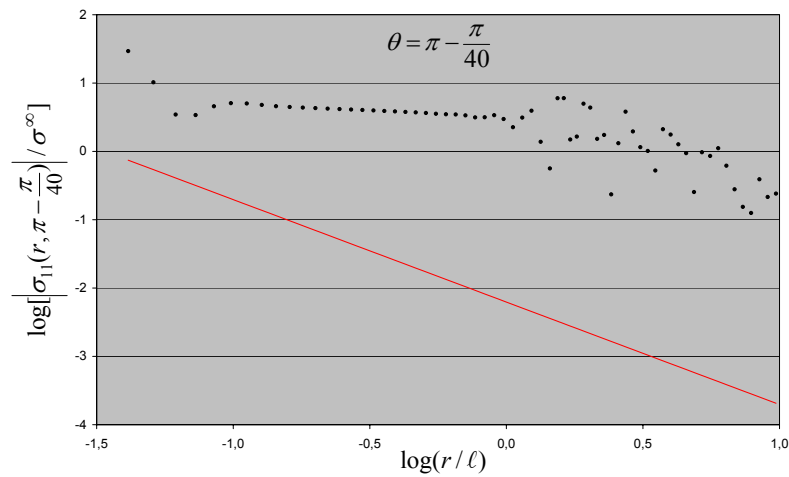

Figure 5.3: Variation of $\log[\left|\sigma_{22}(r, \frac{\pi}{40})\right|/\sigma^{\infty}]$ with $\log \frac{r}{\ell}$ along the radial line $\theta = \frac{\pi}{40}$. The solid line represents the asymptotic crack-tip solution, and the dots the results of the finite element solution.
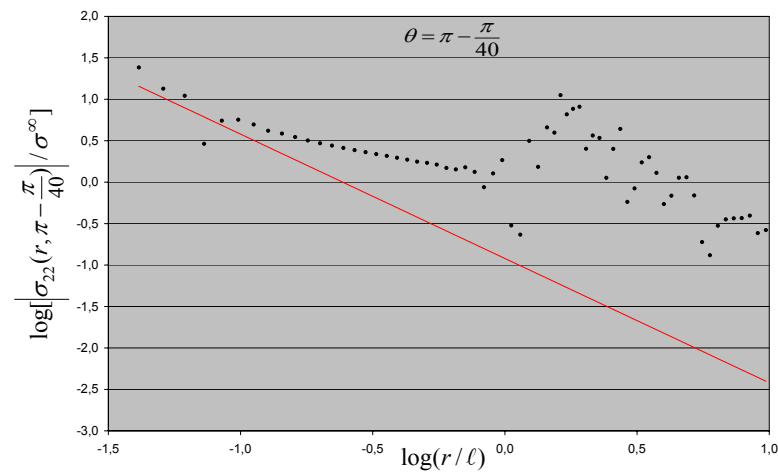
Figure 5.4: Variation of $\log[\left|\sigma_{(12)}(r, \frac{\pi}{40})\right|/\sigma^\infty]$ with $\log\frac{r}{\ell}$ along the radial line $\theta = \frac{\pi}{40}$. The solid line represents the asymptotic crack-tip solution, and the dots the results of the finite element solution.

Figure 5.5: Variation of $\log[\left|\sigma_{[12]}(r, \frac{\pi}{40})\right|/\sigma^\infty]$ with $\log\frac{r}{\ell}$ along the radial line $\theta = \frac{\pi}{40}$. The solid line represents the asymptotic crack-tip solution, and the dots the results of the finite element solution.
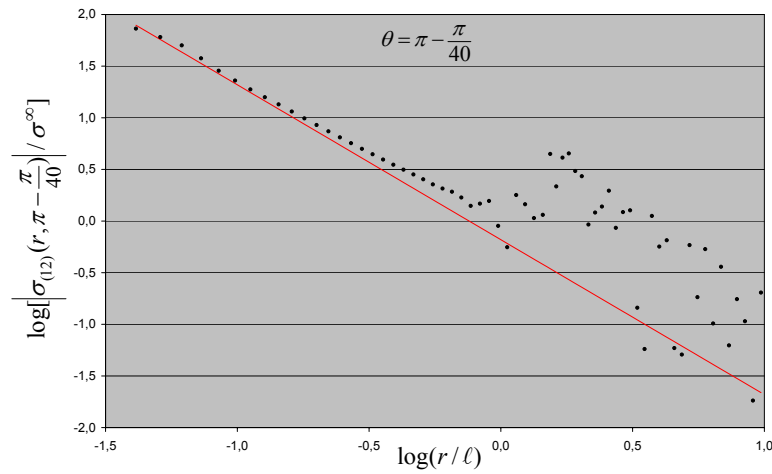
Figure 5.6: Variation of $\log\left[\left|\sigma_{11}(r, \pi - \frac{\pi}{40})\right|/\sigma^{\infty}\right]$ with $\log\frac{r}{\ell}$ along the radial line $\theta = \pi - \frac{\pi}{40}$. The solid line represents the asymptotic crack-tip solution, and the dots the results of the finite element solution.
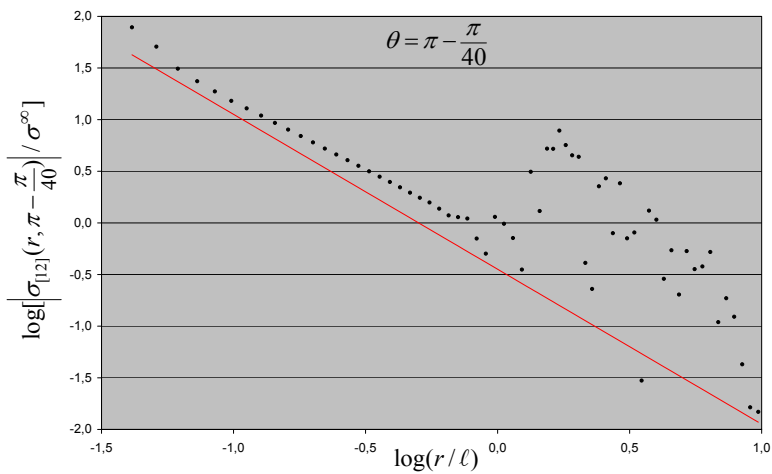

Figure 5.7: Variation of $\log\left[\left|\sigma_{22}(r, \pi - \frac{\pi}{40})\right|/\sigma^{\infty}\right]$ with $\log\frac{r}{\ell}$ along the radial line $\theta = \pi - \frac{\pi}{40}$. The solid line represents the asymptotic crack-tip solution, and the dots the results of the finite element solution.

Figure 5.8: Variation of $\log[\left|\sigma_{(12)}(r, \pi - \frac{\pi}{40})\right|/\sigma^\infty]$ with $\log \frac{r}{\ell}$ along the radial line $\theta = \pi - \frac{\pi}{40}$. The solid line represents the asymptotic crack-tip solution, and the dots the results of the finite element solution.

Figure 5.9: Variation of $\log[\left|\sigma_{[12]}(r, \pi - \frac{\pi}{40})\right|/\sigma^\infty]$ with $\log \frac{r}{\ell}$ along the radial line $\theta = \pi - \frac{\pi}{40}$. The solid line represents the asymptotic crack-tip solution, and the dots the results of the finite element solution.

Figures 5.10-5.13 show the angular variation of the normalized components of σ_{11}, σ_{22}, $\sigma_{(12)}$ and $\sigma_{[12]}$ at various radial distances from the crack-tip together with the corresponding prediction of the asymptotic crack-tip solution. In particular, the angular variation of the following quantities is plotted:

$$\left\{ \frac{\sigma_{11}/\sigma^\infty}{(r/\ell)^{\frac{3}{2}}}, \ \frac{\sigma_{22}/\sigma^\infty}{(r/\ell)^{\frac{3}{2}}}, \ \frac{\sigma_{(12)}/\sigma^\infty}{(r/\ell)^{\frac{3}{2}}}, \ \frac{\sigma_{[12]}/\sigma^\infty}{(r/\ell)^{\frac{3}{2}}} \right\}. \tag{5.2}$$
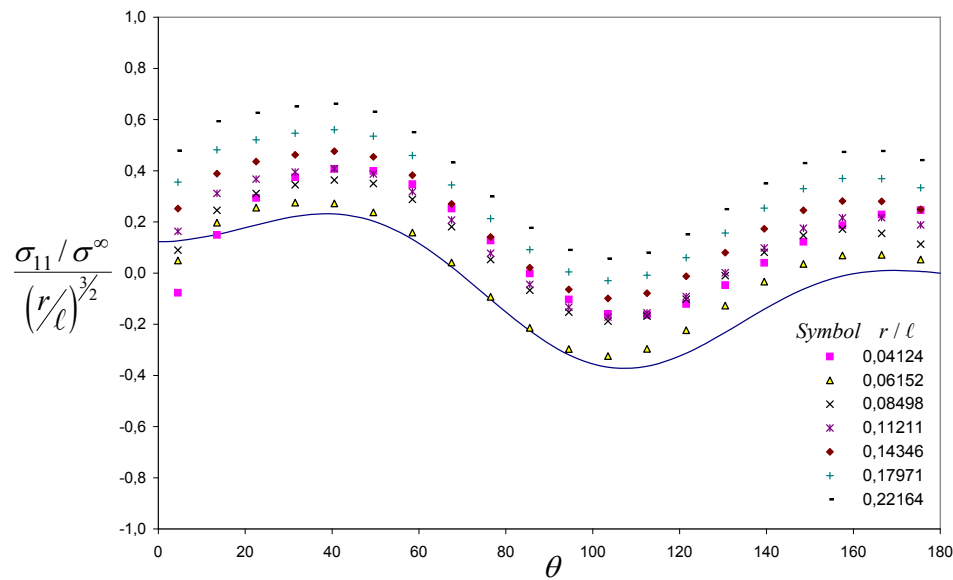
Figure 5.10: Angular variation of the normalized true stress $\frac{\sigma_{11}/\sigma^\infty}{(r/\ell)^{3/2}}$ at various radial distances. The solid line represents the asymptotic crack-tip solution.
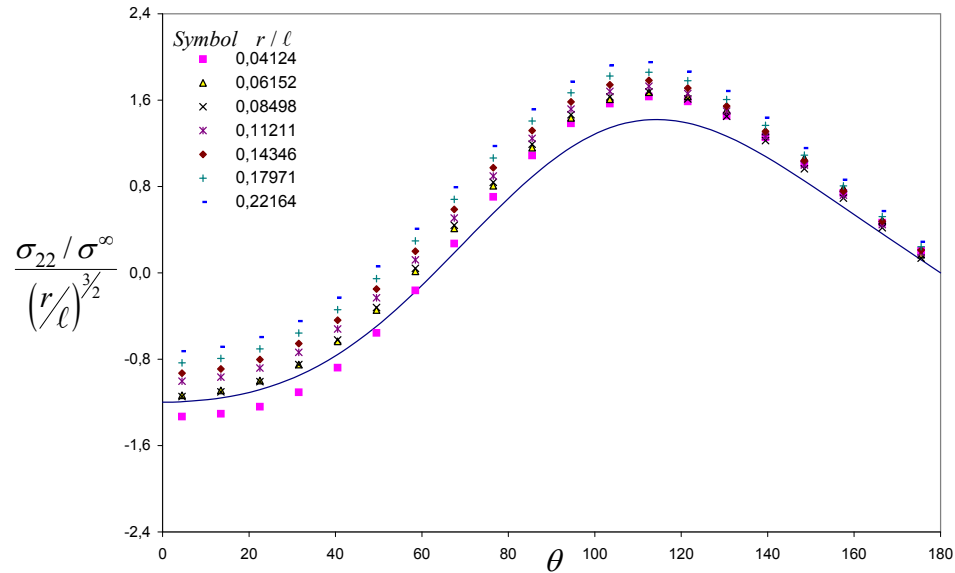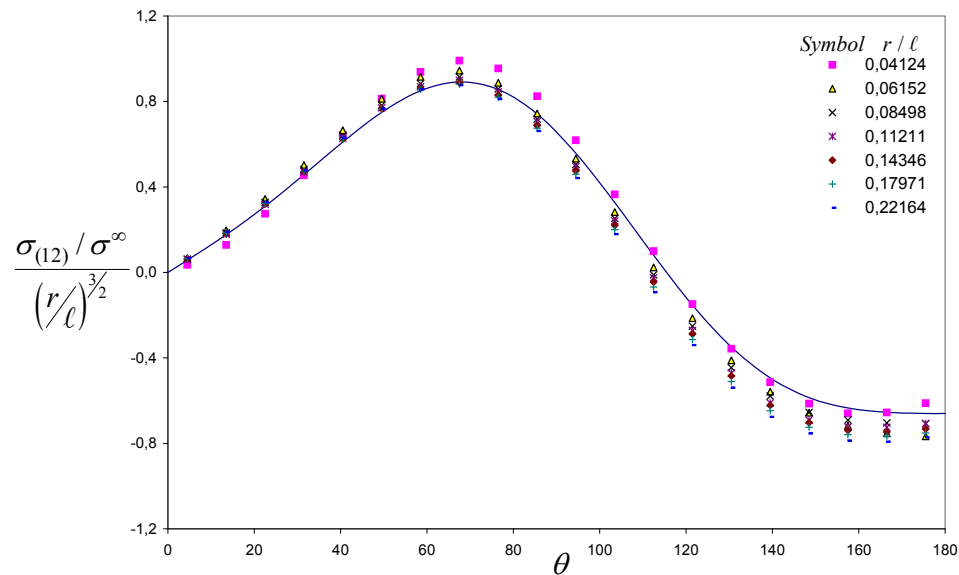
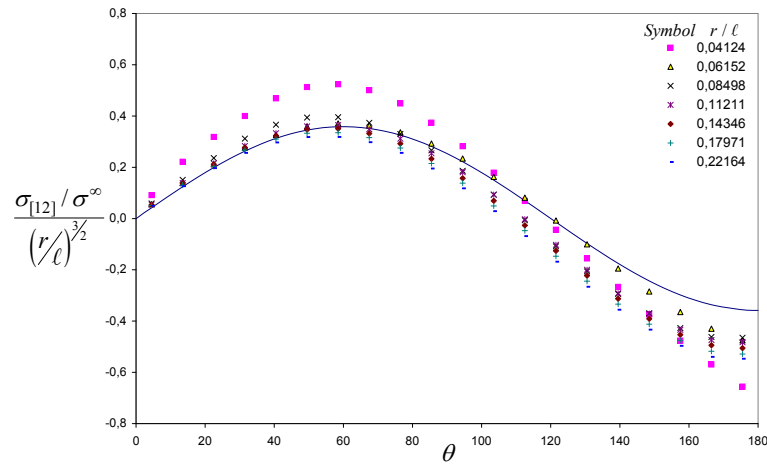Figure 5.11: Angular variation of the normalized true stress $\frac{\sigma_{22}/\sigma^\infty}{\left(\frac{r}{\ell}\right)^{\frac{3}{2}}}$ at various radial distances. The solid line represents the asymptotic crack-tip solution.

Figure 5.12: Angular variation of the normalized true stress $\frac{\sigma_{(12)}/\sigma^\infty}{\left(\frac{r}{\ell}\right)^{\frac{3}{2}}}$ at various radial distances. The solid line represents the asymptotic crack-tip solution.

Figure 5.13: Variation of the normalized true stress $\frac{\sigma_{[12]}/\sigma^\infty}{\left(\frac{r}{\ell}\right)^{\frac{3}{2}}}$ at various radial distances. The solid line represents the asymptotic crack-tip solution.

For the specimen geometry and applied loads considered above, we carry out finite element calculations with $\ell/a = 0., 0.001, 0.01, 0.1$. Again the value $\nu = 0$ is used for Poisson's ratio. For each value of ℓ, two sets of calculations are carried out: one with normalized true stress σ_{22} and another with normalized normal strain ϵ_{22} as a function of the normalized radial distance r, for the gradient and classical elasticity solutions. In the gradient elasticity solution σ_{22} reaches a maximum at $r \simeq \ell$.

Figures 5.14-5.17 show the variation of the normalized true stress $\sigma_{22}/\left(P/W\right)$ as a function of the normalized radial distance r/ℓ along the radial line $\theta = \frac{\pi}{40}$ for both the gradient and classical elasticity solutions.
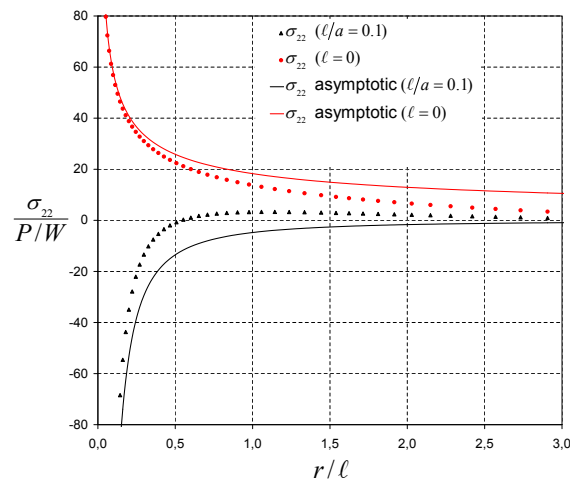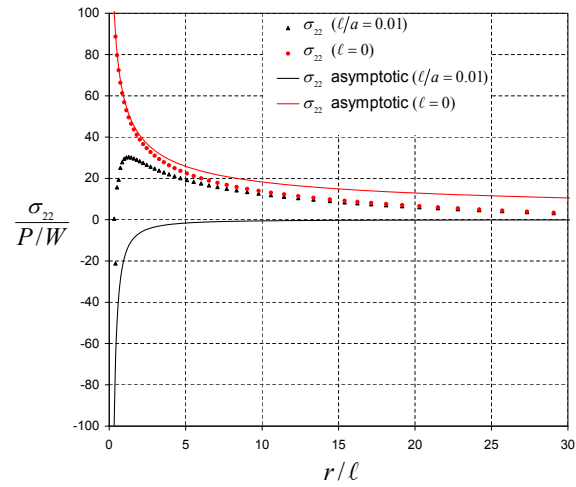

Figure 5.14: Variation of the normalized true stress $\sigma_{22}/\left(P/W\right)$ as a function of the normalized radial distance r/ℓ along the radial line $\theta = \frac{\pi}{40}$ for both the gradient and classical elasticity solutions.

Figure 5.15: Variation of the normalized true stress $\sigma_{22}/(P/W)$ as a function of the normalized radial distance r/ℓ along the radial line $\theta = \frac{\pi}{40}$ for both the gradient and classical elasticity solutions.
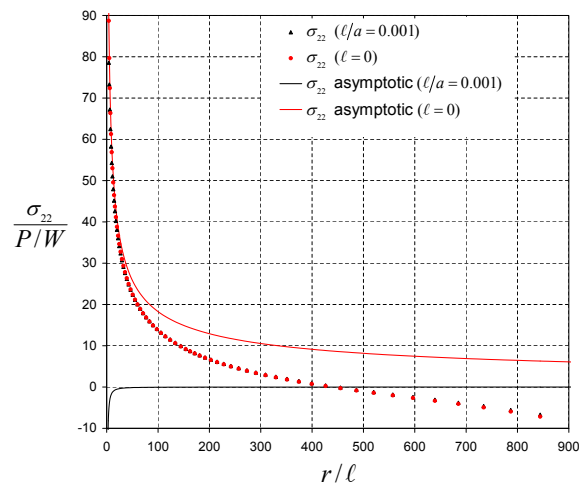

Figure 5.16: Variation of the normalized true stress $\sigma_{22}/(P/W)$ as a function of the normalized radial distance r/ℓ along the radial line $\theta = \frac{\pi}{40}$ for both the gradient and classical elasticity solutions.
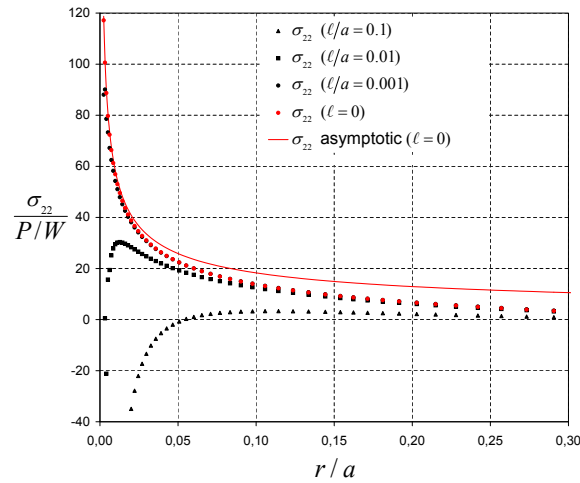
Figure 5.17: Variation of the normalized true stress $\sigma_{22}/(P/W)$ as a function of the normalized radial distance r/a along the radial line $\theta = \frac{\pi}{40}$ for both the gradient and classical elasticity solutions.

Figures 5.18-5.21 show the variation of ϵ_{22} ahead of the crack $(\theta = 0)$ for the gradient and classical elasticity solutions.
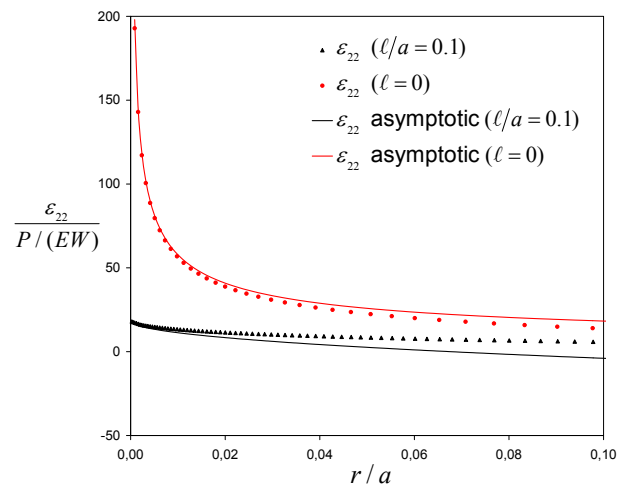

Figure 5.18: Variation of the normalized normal strain $\frac{\epsilon_{22}}{P/(EW)}$ as a function of the normalized radial distance r/a along the radial line $\theta = 0$ for both the gradient and classical elasticity solutions.
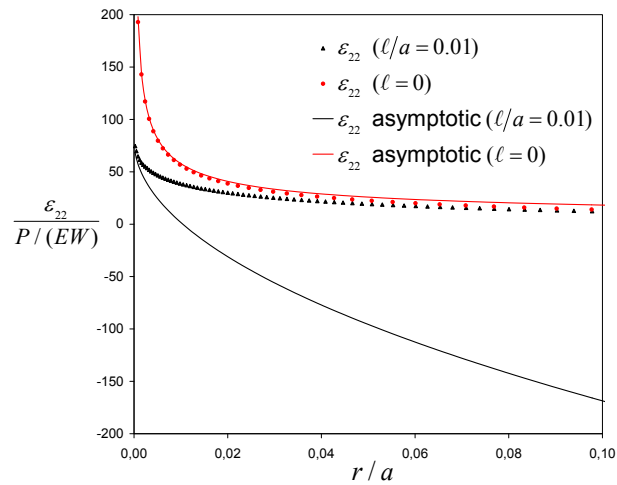
Figure 5.19: Variation of the normalized normal strain $\frac{\epsilon_{22}}{P/(EW)}$ as a function of the normalized radial distance r/a along the radial line $\theta = 0$ for both the gradient and classical elasticity solutions.

Figure 5.20: Variation of the normalized normal strain $\frac{\epsilon_{22}}{P/(EW)}$ as a function of the normalized radial distance r/a along the radial line $\theta = 0$ for both the gradient and classical elasticity solutions.

Figure 5.21: Variation of the normalized normal strain $\frac{\epsilon_{22}}{P/(E\,W)}$ as a function of the normalized radial distance r/a along the radial line $\theta = 0$ for both the gradient and classical elasticity solutions.
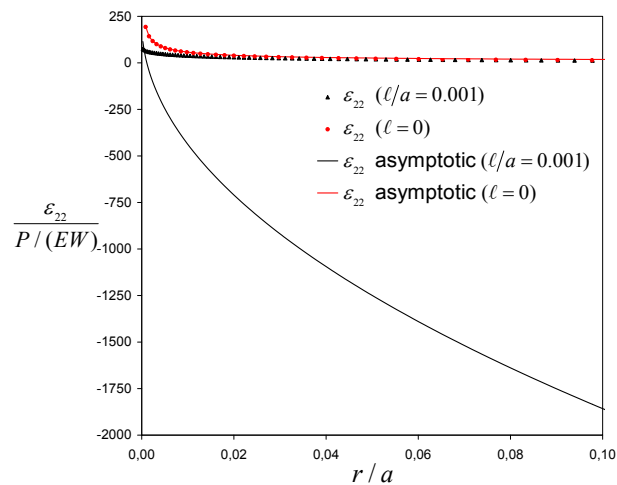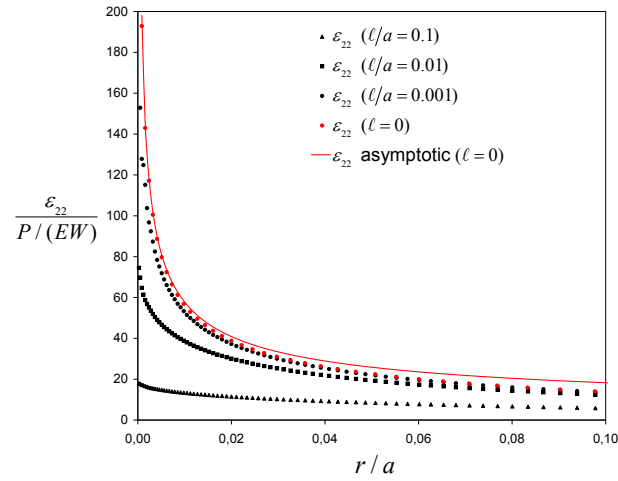
Figures 5.22-5.26 show angular plots of the true stress components at the radial distance that maximizes σ_{22} ahead of the crack ($\ell/a = 0.1$).

Figure 5.22: Angular variation of σ_{11} at the radial distances which $\sigma_{\theta\theta}$ maximizes ahead of the crack. The solid line represents the approximating functional form, and the dots the results of the finite element solution.
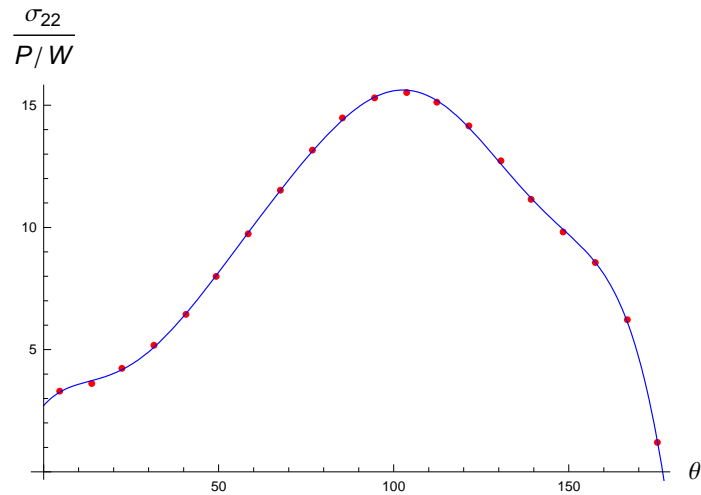
Figure 5.23: Angular variation of σ_{22} at the radial distances which $\sigma_{\theta\theta}$ maximizes ahead of the crack. The solid line represents the approximating functional form, and the dots the results of the finite element solution.
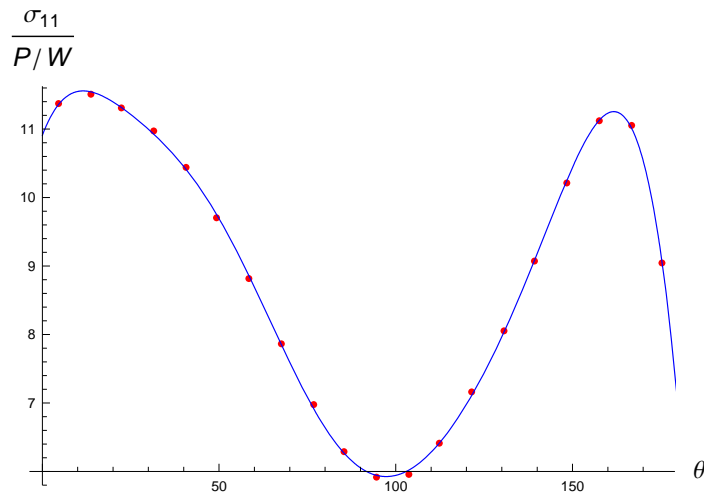

Figure 5.24: Angular variation of σ_{12} at the radial distances which $\sigma_{\theta\theta}$ maximizes ahead of the crack. The solid line represents the approximating functional form, and the dots the results of the finite element solution.

Figure 5.25: Angular variation of σ_{21} at the radial distances which $\sigma_{\theta\theta}$ maximizes ahead of the crack. The solid line represents the approximating functional form, and the dots the results of the finite element solution.
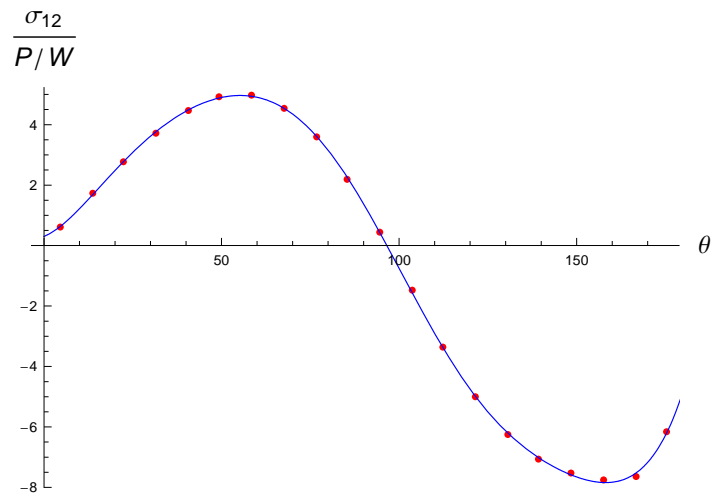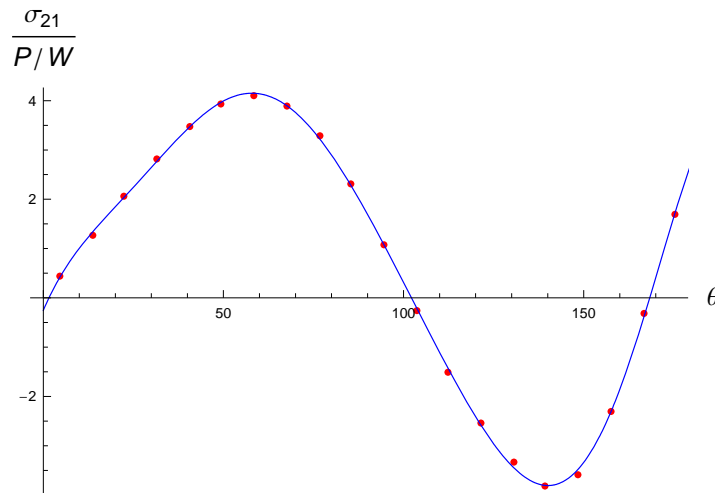
The results shown above can be approximated by the following expressions

$$\frac{\sigma_{11}}{P/W} = -6.41847 + 1.99194\cos\theta + 9.28268\cos 2\theta - 1.48744\cos 3\theta - 0.64241\cos 4\theta +$$

$$+ 14.6615\sin\theta - 2.26578\sin 2\theta - 3.19525\sin 3\theta + 0.35435\sin 4\theta, \tag{5.3}$$

$$\frac{\sigma_{22}}{P/W} = -12.7025 + 3.46502\cos\theta + 13.5931\cos 2\theta - 2.73359\cos 3\theta - 0.94459\cos 4\theta +$$

$$+ 25.4893\sin\theta - 4.961234\sin 2\theta - 5.48417\sin 3\theta + 0.80348\sin 4\theta, \tag{5.4}$$

$$\frac{\sigma_{12}}{P/W} = 5.11345 - 0.1163\cos\theta - 6.19455\cos 2\theta + 0.75721\cos 3\theta + 0.5161\cos 4\theta -$$

$$- 9.16073\sin\theta + 2.03975\sin 2\theta + 2.31792\sin 3\theta + 0.29589\sin 4\theta, \tag{5.5}$$

$$\frac{\sigma_{21}}{P/W} = -3.37529 - 0.47195\cos\theta + 4.17342\cos 2\theta - 0.09338\cos 3\theta - 0.48324\cos 4\theta +$$

$$+ 6.27743\sin\theta + 1.33057\sin 2\theta - 2.1782\sin 3\theta + 0.00493\sin 4\theta. \tag{5.6}$$

The corresponding $\sigma_{\theta\theta}$ is determined from the expression

$$\sigma_{\theta\theta} = \frac{\sigma_{11} + \sigma_{22}}{2} - \frac{\sigma_{11} - \sigma_{22}}{2}\cos 2\theta - \frac{\sigma_{12} + \sigma_{21}}{2}\sin 2\theta. \tag{5.7}$$
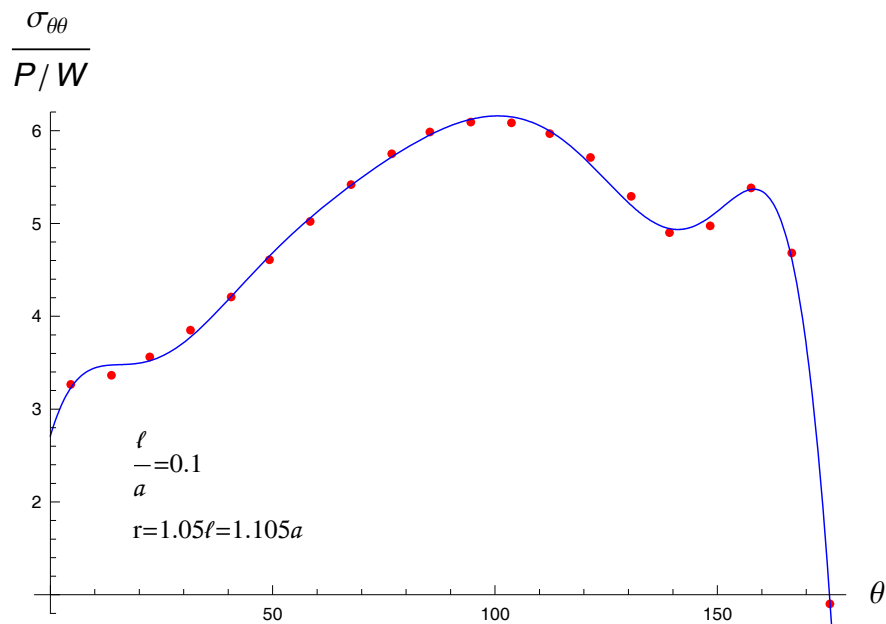
Figure 5.26: Angular variation of the normalized $\frac{\sigma_{\theta\theta}}{P/W}$ at the radial distance at which $\sigma_{\theta\theta}$ maximizes ahead of the crack. The solid line represents the approximating functional form, and the dots the results of the finite element solution.

Figure 5.26 shows the angular variation of $\sigma_{\theta\theta}$. It interesting to note that the maximum value of $\sigma_{\theta\theta}$ does not appear at $\theta = 0$, but appears at $\theta \simeq 100°$!

The results of the finite element calculations are used for the evaluation of the quantities $\tilde{A}, \tilde{B}, \tilde{A}_1, \tilde{A}_2$ in the asymptotic crack-tip solutions (Aravas and Giannakopoulos [2]) and the radial distance $r_{\max}$ at which $\sigma_{\theta\theta}$ maximizes ahead ($\theta = 0$) of the crack (Fig. 5.27) where ℓ is the internal length and a is the crack length of the problem under consideration.

Edge Cracked Panel

ℓ/a	$\tilde{A}_1$	$\tilde{A}_2$	$\tilde{A}$	$\tilde{B}$	$r_{\max}/\ell$
0.001	310.569	364.641	208.720	218.640	3.22
0.01	118.510	137.128	75.694	80.320	1.27
0.1	32.600	40.300	21.120	18.360	1.05
0.2	19.134	23.505	11.104	9.470	0.77

Figure 5.27: Variation of the quantities $\tilde{A}, \tilde{B}, \tilde{A}_1, \tilde{A}_2$ with the normalized radial distance $r_{\max}$ at which $\sigma_{\theta\theta}$ maximizes ahead ($\theta = 0$) of the crack.

Chapter 6

Closure

In this thesis, we considered the plane strain problems of a center-cracked panel (CCP) and an edge-cracked panel (ECP). The specimens and the applied loads were symmetric with respect to the crack plane (mode-I) in both cases.

The problems were solved by using the finite element formulation of Amanatidou and Aravas [1], which was implemented in the ABAQUS general purpose finite element program.

We carried out detailed finite element calculations and we proceeded comparing the results with the asymptotic crack-tip solutions developed by Aravas and Giannakopoulos [2].

The region of dominance of the asymptotic solution for the CCP geometry analyzed were found to be of order $\ell/10$ which is in accord to what has been reported by Aravas and Giannakopoulos [2] for the ECP geometry.

In order to validate our results we calculated Cartesian components of the true stresses for both specimens. Results were presented in the form of diagrams and verified the corresponding asymptotic crack-tip solutions developed by Aravas and Giannakopoulos [2].

Bibliography

[1] E. Amanatidou and N. Aravas, 'Mixed finite element formulations of strain-gradient elasticity problems', *Comp. Methods Appl. Mech. Eng.* **191** (2002) 1723–1751.

[2] N. Aravas and A. E. Giannakopoulos, 'Plane asymptotic crack tip solutions in gradient elasticity', *Int. J. Solids Struct.* **46** (2009) 4478–4503.

[3] Cosserat, E. et Cosserat, F., *Théorie des Corps Déformables*, Librairie Scientifique A. Hermann et Fils, Paris, 1909 (english translation *Theory of Deformable Bodies*, National Aeronautics and Space Administration (NASA) TT F-11 561, Washington D.C., February 1968).

[4] G. E. Exadaktylos, 'On the problem of the circular hole in an elastic material with microstructure', private communication (2001).

[5] I. D. Gavardinas, 'Connecting far-field loading with intensity of tractions and displacements at the Mode I crack-tip for strain-gradient elastic materials', MSc Thesis, Department of Civil Engineering, University of Thessaly, 2007.

[6] H. Georgiadis, 'Exact analysis of crack-tip fields in gradient-elastic anti-plane shear deformation', *Recent Advances in Mechanics*, Honorary Volume for Prof. A. N. Kounadis, edited by J. T. Katsikadelis, D. E. Beskos and E. E. Gdoutos, pp. 263-272, National Technical University of Athens, 2000.

[7] P. Germain, 'Sur l'application de la méthode des puissances virtuelles en mécanique des milieux continus', *C. R. Acad. Sc. Paris* **274** (1972) 1051-1055.

[8] P. Germain, 'The method of virtual power in Continuum Mechanics. Part 2: Microstructure', *SIAM J. Appl. Math.* **25** (1973) 556-575.

[9] P. Germain, 'La méthode des puissances virtuelles en mécanique des milieux continus', *J. Mécanique* **12** (1973) 235-274.

[10] W. T. Koiter, 'Couple-stresses in the theory of elasticity. I', *Proc. K. Ned. Akad. Wet. (B)* **67** (1964) 17–29.

[11] W. T. Koiter, 'Couple-stresses in the theory of elasticity. II', *Proc. K. Ned. Akad. Wet. (B)* **67** (1964) 30–44.

[12] G. F. Karlis, S. V. Tsinopoulos, D. Polyzos and D. E. Beskos, 'Boundary element analysis of mode I and mixed mode (I and II) crack problems of 2-D gradient elasticity', *Comp. Methods Appl. Mech. Eng.* **196** (2007) 5092–5103.

[13] G. F. Karlis, S. V. Tsinopoulos, D. Polyzos and D. E. Beskos, '2D and 3D boundarey element analysis of mode-I cracks in gradient elasticity', *Comp. Model. Engng & Sci.* **28** (2008) 189–207.

[14] R. D. Mindlin, 'Microstructure in linear elasticity', *Archs Ration. Mech. Anal.* **10** (1964) 51–78.

[15] R. D. Mindlin, 'Second gradient of strain and surface tension in linear elasticity', *Int. J. Solids Struct.* **1** (1965) 417–438.

[16] R. D. Mindlin and N. N. Eshel, 'On first-gradient theories in linear elasticity', *Int. J. Solids Struct.* **4** (1968) 109–124.

[17] R. D. Mindlin and H. F. Tiersten, 'Effects of couple-stresses in linear elasticity', *Archs Ration. Mech. Anal.* **11** (1962) 415–448.

[18] R. D. Mindlin, 'Stress functions for a Cosserat Continuum', *Int. J. Solids Struct.* **1** (1965) 265–271.

[19] R. A. Toupin, 'Elastic materials with couple-stresses', *Archs Ration. Mech. Anal.* **11** (1962) 385–414.

[20] L. Zhang, Y. Huang, J. Y. Chen and K. C. Hwang, 'The mode III full-field solution in elastic materials with strain gradient effects', *J. Mech. Phys. Solids* **44** (1998) 1621–1648.

[21] O. C. Zienkiewicz and R. L. Taylor, *The Finite Element Method*, 5th edition, Butterworth-Heinemann, 2000.